Turbulent transport and reactions of plant-emitted hydrocarbons in an Amazonian rain forest

Jose D Fuentes[a,*], Tobias Gerken[a], Marcelo Chamecki[b], Paul Stoy[1], Livia Freire[a], Jesus Ruiz-Plancarte[a]

[a] *Department of Meteorology and Atmospheric Science, The Pennsylvania State University, University Park, PA*
[b] *Department of Atmospheric and Oceanic Sciences, University of California, Los Angeles, CA*

Abstract

The processes governing the temporal and spatial patterns of isoprene and monoterpenes emitted by a rainforest in the central Amazon region of Brazil is investigated using a combination of field experiments and numerical simulations. Specifically, Large Eddy Simulations (LES) are used to resolve emissions of isoprene and monoterpenes, turbulent transport, and air chemistry. The coupled chemistry-transport LES included the effects of isoprene and monoterpenes reactivity due to reactions with hydroxyl radical and ozone. The LES results are used to compute vertically resolved budgets of isoprene and monoterpenes in the rainforest canopy in response to emissions, turbulent transport, surface deposition, and air chemistry. Results indicated that emission and dispersion dominated the isoprene budget as the gases were transported out of the canopy space. In a region limited by nitrogen oxides (with prevailing nitric oxide levels of < 0.5 parts per billion), the in-canopy chemical destruction removed approximately 10% of locally emitted monoterpenes. Hydroxyl radical production rates from the ozonolysis of monoterpenes amounted to $\approx 2 \times 10^6$ radicals $\mathrm{cm}^{-3}\,\mathrm{s}^{-1}$ and had similar magnitude to the light-dependent hydroxyl radical formation. One key conclusion was that the Amazonia rainforest abundantly emitted monoterpenes whose in-canopy ozonolysis yielded hydroxyl radicals in amounts similar to the magnitude of light-dependent formation. Reactions of monoterpenes and isoprene with hydroxyl radical and ozone were necessary for the maintenance of the Amazon rainforest canopy as a photochemically active environment suitable to generate oxidants and secondary organic aerosols.

*Corresponding author
Email address: jdfuentes@psu.edu (Jose D Fuentes)

1. Introduction

The Amazon rainforest represents the most expansive and contiguous region of the world with the largest and the most diverse emissions of biogenic volatile organic compounds (BVOCs) (Jardine et al., 2011, 2015a,b). Due to the suitable environmental conditions to promote productive biosynthesis and emissions – namely high air temperature ($> 20\ ^{o}$C) and sunlight – the rainforest releases isoprenoid molecules year round (Arneth et al., 2011; Sindelarova et al., 2014). Plants in the Amazon emit rich blends of BVOCs that are mostly comprised of isoprene (C_5H_8), monoterpenes ($C_{10}H_{16}$), sesquiterpenes ($C_{15}H_{24}$), and oxygenated compounds such as methanol (CH_3OH) (Jardine et al., 2011, 2015a). Because of strong sources, isoprene and monoterpenes can reach maximum ambient mixing ratios of 20 and 2 parts per billion (ppb) on a volume basis, respectively, with some seasonality in emissions due to foliage ontogeny (Alves et al., 2016; Wei et al., 2018; Yáñez-Serrano et al., 2018).

In the tropical atmospheric boundary layer (ABL) overlying the rainforest, the observed large hydroxyl radical (HO) reactivities arise from the abundant emissions of BVOCs (Edwards et al., 2013; Nölscher et al., 2016; Pfannerstill et al., 2021). In response to the pletora of emitted reactive chemical species, the HO budget in the ABL is adjusted by BVOC levels (Liu et al., 2016, 2018). This influence occurs because the principal sink of isoprene is its reaction with HO. The oxidation of isoprene generates hydroperoxy aldehydes (HPALD) whose rapid photolysis results in a first-generation of hydroperoxyl radical (HO_2) and HO (Taraborrelli et al., 2012; Fuchs et al., 2013; Rohrer et al., 2014; Bates and Jacob, 2019; Schwantes et al., 2020). In addition, ozonolysis of monoterpenes (Atkinson et al., 1992; Aschmann et al., 2002; Herrmann et al., 2010) produces relatively high yields of HO, thereby contributing to the oxidation capacity of the tropical ABL (Lelieveld et al., 2008; Whalley et al., 2011). In general, the reactions of BVOCs with ozone (O_3), HO, and nitrate radical (NO_3) contribute to the formation of additional oxidants (e.g., organic peroxide radicals) and secondary organic aerosols (SOAs) (Fuentes et al., 2000; Pöschl et al., 2000, 2010). Therefore, BVOCs can indirectly play critical roles in cloud formation processes (Pöschl et al., 2010) and regional climate (Barr et al., 2003). Despite the recent progress in discerning the chemical cycles of BVOCs, additional investigations are still required to determine (i) the mechanisms governing their turbulent transport from the biosphere to the ABL and (ii) the ensuing chemistry under the influences of varying levels of nitrogen oxides (NOx).

Turbulence is the primary agent transporting BVOCs and associated chemical processes occurring within and above the rainforest canopy. During the daytime, only the upper half of the rainforest canopy is well mixed whereas its lower region is either partially or poorly mixed due to the effective momentum sink in the forest crown (Fitzjarrald et al., 1990; Kruijt et al., 2000; Gerken et al., 2017). For the most part, the rainforest canopy remains poorly mixed at night due to buoyancy destruction of mechanically produced turbulence (Fitzjarrald and Moore, 1990; Santos et al., 2016; Freire et al., 2017). Turbulence characteristics give rise to median canopy residence times that can approach 30 minutes in the lower canopy layers under statically neutral conditions (Gerken et al., 2017). Because such air parcel residence times are comparable to lifetimes of many BVOCs (Fuentes et al., 2000), appreciable amounts can undergo reactions before they are vented out of the forest environment. Furthermore, the transport of BVOCs is impacted by sweeps and ejections from coherent mixing-layer eddies (Raupach et al., 1996; Finnigan, 2000) whose penetration depth into the canopy is limited by the dense Amazon plant canopy (Fitzjarrald et al., 1990; Kruijt et al., 2000). The need to explore turbulent transport and chemistry in concert is further highlighted as air parcels emanating from the canopy are enriched with plant-emitted hydrocarbons as descending air motions transport O_3 and other atmospheric oxidants into the canopy airspace (Fuentes et al., 2007; Gerken et al., 2016; Freire et al., 2017).

Large Eddy Simulations (LES) can provide realistic estimates of the links between the turbulence features in both the plant canopy and the atmospheric boundary layer, and the chemistry of isoprene and monoterpenes, which are ordinarily under resolved in most regional models. Early LES studies involving plant canopies applied to passive scalars (Shaw and Schumann, 1992; Edburg et al., 2011) and treated reactive gases (Patton et al., 2001) based on their exponential decays due to chemical reactions. Recent LES investigations coupled condensed (Vilà-Guerau de Arellano et al., 2011; Ouwersloot et al., 2013) and detailed (Su et al., 2016; Khan et al., 2021) photochemical mechanisms with atmospheric turbulence to determine the oxidation of isoprene in convective boundary layers, but did not include in-canopy chemical reactions. Patton et al. (2016) integrated canopy and convective boundary-layer processes to link turbulence and scalars, emphasizing the potential to extend the LES approach to include photochemical mechanisms necessary for studying detailed chemical reactions of BVOCs in forest canopies. In addition, stochastic Lagrangian transport models (Strong et al., 2004; Rinne et al., 2012) have been applied to determine the reactions

isoprene and monoterpenes with oxidants as first order decay in and above forest canopies.

Building on these earlier studies, this investigation was framed around three objectives. First, we determined the processes governing temporal and spatial patterns of isoprene and monoterpenes in response to emissions, turbulent transport, surface dry deposition, and chemical reactions. Second, we estimated the fraction of locally emitted isoprene and monoterpenes destroyed in the rainforest canopy due to surface deposition and chemical reactions occurring under the influences of observed O_3 and nitric oxide (NO) levels. Third, given the substantial daytime concomitant emissions of isoprene and monoterpenes in the rainforest, we ascertained the feedback generated between ozonolysis of monoterpenes and chemical destruction of isoprene via its reaction with HO. To achieve these objectives, we included in an updated LES the algorithm for the explicit treatment of chemical reactions to resolve turbulent transport of mass, energy, and momentum in and above a rainforest canopy.

2. Methodology

2.1. Study site description and field measurements

Field data used here were collected during April 2014 to January 2015 (Fuentes et al., 2016). The study site is located approximately 60 km north-northwest of Manaus, Amazonas, Brazil. The site consists of dense primary rainforest with a canopy height (h_c) of approximately 35 m. The leaf area index (LAI) ranged from 5.7 to 7.3 m^2 m^{-2} (McWilliam et al., 1993; Marques Filho et al., 2005; Tota et al., 2012), depending on the location of measurements. Terrain consists of gentle valleys and hills. A 50-m meteorological tower is located on an approximately 60-m high plateau. Located in the middle of the forest, the tower served as the platform to mount nine triaxial sonic anemometers (CSAT-3, Campbell Scientific Inc, Logan, UT) to measure the three wind components (u, v, and w), their turbulent fluctuations, and the sonic temperature at 20 Hz. Measurement heights were $z\,h_c^{-1}$ = 1.38, 1.15, 1.0, 0.90, 0.70, 0.63, 0.52, 0.39, and 0.20. One additional sonic anemometer was placed near the tower at $z\,h_c^{-1} = 0.04$. Mean air relative humidity and temperature (HMP-155, Vaisala, Vantaa, Finland) were measured at the 32-m height. Ambient O_3 mixing ratios (49i, Thermo Fisher Scientific, Waltham, MA) were measured at a frequency of 1 Hz. A Proton Transfer Reaction Mass Spectrometer (PT-RMS, Ionicon Analytik, Innsbruck, Austria) measured isoprene, aggregated monoterpene, and the sum of methyl-vinyl ketone and methacrolein

(MVK+MACR) mixing ratios. Both instruments shared a common gas sampling inlet equipped with a rain-shield and placed at $z\,h_c^{-1} = 1.14$ and were housed in a temperature-controlled shed, located 5 m from the tower. Air samples were drawn at a rate of $12\,\mathrm{L\,min^{-1}}$ through a 1-μm pore size Teflon filter and through a 3/8-inch outer diameter Teflon tube that was shielded from sunlight. Photosynthetically active radiation (PAR) was measured at $z\,h_c^{-1} = 1.46$, and air temperature was recorded at $z\,h_c^{-1} = 1.46, 1.21, 0.8, 0.44, 0.15$. Ambient air pressure as well as turbulent fluxes of sensible and latent heat ($z\,h_c^{-1} = 1.46$) were averaged in 30-minute intervals. Additional details on the study site, measurements, and postprocessing of data are provided elsewhere (Fuentes et al., 2016).

2.2. Large Eddy Simulation

A description of the governing equations and the main features of the LES are provided here and additional details are reported elsewhere (Chamecki et al., 2008, 2009; Pan et al., 2014). For incompressible flows ($\nabla \cdot \tilde{\mathbf{u}} = 0$), the filtered momentum and air mass conservation equations were solved to obtain the three dimensional wind field ($\tilde{\mathbf{u}}$):

$$\frac{\partial \tilde{\mathbf{u}}}{\partial t} + (\tilde{\mathbf{u}} \cdot \nabla)\,\tilde{\mathbf{u}} = -\frac{1}{\rho}\nabla\,(\tilde{p} + P) - \mathbf{g}\left(\frac{\tilde{\theta}_v - \langle\tilde{\theta}_v\rangle}{\langle\tilde{\theta}_v\rangle}\right) - \nabla \cdot \tau_{\mathrm{sgs}} - \mathbf{d}. \tag{1}$$

Terms on the right hand side of Equation (1) represent the resolved pressure gradient force, buoyancy force, subgrid-scale (SGS) force, and the drag force exerted by the forest canopy (represented as a porous medium with negligible fractional solid volume). Hereafter, ρ is air density, $\tilde{p}$ is resolved modified pressure (as it also includes the SGS turbulent kinetic energy), P is the mean pressure used to impose a mean pressure gradient to drive the flow, $\tilde{\theta}_v$ is virtual potential temperature, $\mathbf{g}$ is the gravitational acceleration, τ_{sgs} is the SGS stress tensor, and angle brackets indicate average over horizontal planes. Following Shaw and Schumann (1992), the canopy drag ($\mathbf{d}$) was determined as

$$\mathbf{d} = C_d\ \ (\mathbf{P}\ a(z)) \cdot (|\tilde{\mathbf{u}}|\tilde{\mathbf{u}})\,, \tag{2}$$

where C_d is a constant drag coefficient (form drag), $\mathbf{P}$ is a diagonal tensor that projects the total leaf area density onto planes perpendicular to each of the three spatial dimensions (Pan et al., 2014), and $a(z)$ is the plant area density assumed to be reasonably approximated by the leaf area density. This study assumed a random orientation of leaves ($P_x = P_y = P_z = 1/2$) and a horizontally

homogeneous distribution of LAI for each layer with $C_d = 0.4$. The temporal change of virtual potential temperature $\tilde{\theta}_v$ was expressed as a filtered advection-diffusion equation

$$\frac{\partial \tilde{\theta}_v}{\partial t} + \nabla \cdot (\tilde{\mathbf{u}}\, \tilde{\theta}_v) = -\nabla \cdot \pi_{\theta_\mathbf{v}} + H, \tag{3}$$

where π_{θ_v} is the SGS buoyancy flux, and H is a source term representing the total buoyancy flux from the forest canopy to overlying air layers. Similarly, filtered advection-diffusion-reaction equations were solved for each gaseous chemical species, $\tilde{\chi}_i$

$$\frac{\partial \tilde{\chi}_i}{\partial t} + \nabla \cdot (\tilde{\mathbf{u}}\, \tilde{\chi}_i) = -\nabla \cdot \pi_{\chi_i} + C_i + E_i - D_i, \tag{4}$$

where $\pi_{\chi_\mathbf{i}}$ is the SGS flux for the chemical species, C_i represents the gas net loss or gain due to chemical reactions, and E_i and D_i represent gas emission and deposition, respectively. The filtered equations were closed through SGS momentum fluxes that were determined using the scale dependent Lagrangian dynamic Smagorinsky model (Bou-Zeid et al., 2004). Scalar SGS-fluxes were estimated based on the SGS eddy viscosity and a constant SGS Schmidt number ($\mathrm{Sc}_\tau = 0.8$). Equations (1) and (3) were discretized using a pseudo-spectral approach in the horizontal directions and a second-order centered finite-difference scheme in the vertical. Equations for the gases were discretized using the finite volume method with the third-order upwind advection scheme SMART (Gaskell and Lau, 1988). The time integration of the LES was advanced through the second-order Adam-Bashforth scheme (Peyret and Taylor, 2012). Lateral boundary conditions were periodic for momentum and all scalars. The upper boundary condition was no-stress/no-flux while a wall model based on Monin-Obukhov similarity (Foken, 2006) was used for the lower boundary condition situated at the forest floor.

2.2.1. Emissions of biogenic hydrocarbons

The Model of Emissions of Gases and Aerosols from Nature (MEGAN) version 2.1 (Guenther et al., 2012) was used to estimate emissions of isoprene and monoterpene as a function of leaf area density, temperature, and PAR in the canopy. Vertically resolved emissions ($\mathrm{E}_i(\mathrm{z})$) for a given gas species (i) were estimated for each plant functional type using (Guenther et al., 2006):

$$E_i(z) = C_{\mathrm{ce}}\ \epsilon_i\ \gamma_P(z)\ \gamma_T(z)\ \gamma_A\ \gamma_{SM}\ \gamma_{CO_2}\ a(z). \tag{5}$$

In Equation (5), C_{ce} is a canopy environment model dependent factor (here $C_{\mathrm{ce}} = 0.17$ is adopted to adjust emissions to observed ambient gas levels (Kuhn et al., 2007; Karl et al., 2007)), ϵ_i is

a plant species specific emission factor. The $\gamma_P(z)$ and $\gamma_T(z)$ functions consider the influences of PAR and temperature on emissions of isoprene and monoterpenes. As documented by previous field studies (Rinne et al., 2002; Kuhn et al., 2002; Jardine et al., 2015a), in the Amazon emissions of monoterpenes also depend on PAR levels. The activity factors of leaf age (γ_A), soil moisture (γ_{SM}), and carbon dioxide inhibition on hydrocarbon emissions(γ_{CO_2}) were assumed to equate unity as done by Alves et al. (2016). The vertically resolved temperature and PAR functions, $\gamma_T(z)$ and $\gamma_P(z)$, modulating basal emissions were calculated following Equations (3–11) in Guenther et al. (2012). A two-stream radiative transfer module (Sellers, 1985; Gu, 1999; Moon et al., 2020) was used to estimate PAR for shaded and sunlit leaves. Fractions of sunlit leaves were determined assuming exponential decreases in such foliage with cumulative leaf area as in Dai et al. (2004). Basal emission of isoprene was based on $\epsilon_{\mathrm{Iso}} = 7.0\,\mathrm{mg\,m^{-2}\,h^{-1}}$ and emissions of monoterpenes were calculated as the sum of eight monoterpenes listed in the MEGAN formulation (Guenther et al., 2012) and identified in the studied forest canopy (Jardine et al., 2015a). Emission profiles (Figures 1) were calculated using Equation (5) every 30 minutes during the day and linearly interpolated for times in between. To avoid the repeated execution of the canopy radiative transfer algorithm within the LES, the BVOC emissions were computed offline and externally imposed on the LES.

2.2.2. Summary of reactions involving isoprene and monoterpenes

The third research objective was achieved by estimating the oxidation of isoprene and monoterpenes in and above the rainforest canopy, utilizing a condensed photochemical mechanism (Table S1). Based on the initial gas concentrations, the mechanism calculates formation and destruction of HO, NO_3, and O_3 due to photooxidation of BVOCs. The HO initiates the oxidation of isoprene (ISOP) and monoterpenes (MON), resulting in the formation of peroxyl radicals (RO_2, TPO_2), R9 and R28. As done in previous studies (Van Stratum et al., 2012), the reaction of ISOP with O_3 is not included in the chemical mechanism due to the extremely low reaction coefficient ($k_{O_{3,\mathrm{Iso}}} = 1.30 \times 10^{-17}\,\mathrm{cm^3\,molec^{-1}\,s^{-1}}$). Monoterpenes also react with NO_3 to form free radicals (TPO_2), R30. The ozonolysis of monoterpenes generates HO, methyl vinyl keone (MVK), and hydroperoxyl radicals (HO_2), see R29 in Table S1. The RO_2 and TPO_2 are short-lived and in the presence of NO can produce NO_2, HO_2, MVK, HO, and formaldehyde (CH_2O), R15 and R31. Additional reactions involving MVK with HO generate HO_2 and CH_2O, R10, which can undergo photolysis to generate HO_2, R6. Also, the reaction of CH_2O with HO produces HO_2, R16, which

subsequently combines with NO to generate HO plus NO_2. In low-NO environments (i.e., [NO] < 30 parts per trillion (ppt)), the HO_2 can react with O_3 to form HO whereas the reaction of HO_2 with NO dominates and produces HO and NO_2 in NO-laden air masses (Atkinson, 2000). The photolysis of NO_2 generates NO and ground-triplet state atomic oxygen ($O(^3P)$), which readily combines with O_2 to produce O_3, R5. Therefore, this summary of reactions (R9 to R34) indicates that one key role of BVOCs is to convert NO to NO_2, which is the key precursor of O_3. The condensed photochemical mechanism (Table S1) is an enhanced version of the one described in Heus et al. (2010) and tested for isoprene chemistry in numerical simulations applied above the Amazon rainforest (Vilà-Guerau de Arellano et al., 2011). The isoprene mechanism is based on the one reported by Geiger et al. (2003) and Ouwersloot et al. (2013). Monoterpenes are represented as a single chemical species as implemented in the Model for Ozone and Related chemical Tracers (MOZART) version 4 (Emmons et al., 2010) and used by Su et al. (2016). An implicit two-step chemical solver is applied to estimate rates of reactions (Verwer, 1994; Verwer and Simpson, 1995). Vilà-Guerau de Arellano et al. (2011) and Su et al. (2016) reported that equilibrium HO concentrations in the current chemical mechanism are 30–50% higher than in the more complete chemical mechanisms due to the unaccounted NO_x sinks in species such organic nitrates ($RONO_2$).

2.3. Numerical simulation setup

The modeling domain was $3584 \times 1792 \times 1120\,\mathrm{m}^3$ and was discretized by $164 \times 82 \times 320$ grid points in the streamwise, crosswise, and vertical direction, respectively. The vertical resolution was set as $\Delta z = 3.5\,\mathrm{m}$, which yielded ten layers in the canopy. The horizontal model resolution was $\Delta x = \Delta y = 21.85\,\mathrm{m}$, which corresponded to an aspect ratio of $\Delta x/\Delta z = 2\pi$. The simulation time step was 0.04 s and the chemical mechanism was called every 8 simulation steps. The Coriolis effect was neglected due to the field site's proximity to the Equator. The LAI was set to 6.0 using the vertical leaf area distribution measurements (Tota et al., 2012). Simulations were forced by imposing time dependent mean pressure gradient and heat sources designed to match observed conditions. Simulations from 6:00 h (sunrise) to 12:00 h (all times are given in local time) on 21 September 2014 are included in this manuscript. After sunrise, the pressure gradient driving the flow increased so that diurnal cycle of the friction velocity (u_*) at the canopy top closely matched observed values. The mean pressure gradient was determined from the mean force balance $dP/dx = \rho u_*^2/Z_i$ (Z_i is the depth of the convective boundary layer). Due to the time lag required for the flow field to respond

to changes in the pressure gradient forcing, the time evolution of the forcing had to be adjusted (see Supplement for details). Vertically-resolved kinematic heat fluxes ($\overline{w'\theta'_v}$) from eddy covariance measurements were temporally smoothed (using a linear fit) and vertically interpolated to the numerical grid levels to produce buoyancy fluxes, $B_{\mathrm{smooth}}(z,t)$. In the lower half of the canopy ($z/h_c < 0.5$) fluxes were set to zero as observed daytime fluxes were negligible. The heat source, H, in Equation (3) was specified as $H(z,t) = B_{\mathrm{smooth}}(z,t)/dz$. Similarly to H, the in-canopy water vapor source was specified assuming a constant Bowen ratio in the vertical as determined from above-canopy measurements (Fuentes et al., 2016).

Upper air sounding data taken at a site 20 km away from the tower were used to initialize the LES. The θ_v profile was constant for the first 50 m above ground and then θ_v increased by the gradient of $\partial\theta_v/\partial z = 0.024\,\mathrm{K\,m^{-1}}$ between 50 and 150 m and $\partial\theta_v/\partial z = 0.016\,\mathrm{K\,m^{-1}}$ above 150 m. The initial surface temperature was set to 299 K and the specific humidity profile was set to $17.0\,\mathrm{g\,kg^{-1}}$ below 150 m and $13.0\,\mathrm{g\,kg^{-1}}$ above 150 m. Ozone levels were initialized at 8 ppb at the surface and then linearly increased by $0.056\,\mathrm{ppb\,m^{-1}}$ until they reached a constant level above 450 m. Concentrations of chemical species were initialized as constant values within the entire domain (a value of zero was chosen unless indicated in Table 1). Due to the unpolluted conditions at the study site, NO_2 was set to 0.1 ppb with 0.1 ppb of NO near the surface. The soil NO source of $5 \times 10^{-4}\,\mathrm{ppb\,m\,s^{-1}}$ was considered (Vilà-Guerau de Arellano et al., 2011). Ozone deposition to the canopy was modeled following Wolfe and Thornton (2011). Isoprene deposition to the ground surface was considered through a deposition velocity, $V_{\mathrm{dep}} = 2.7\,\mathrm{mm\,s^{-1}}$ (Gordon et al., 2014). At the ground, zero flux of monoterpenes was assumed. Three numerical simulations were performed. The first simulation (hereafter labeled as *Iso*) included emissions and chemistry of isoprene only (R1 – R27, Table S1). The *Iso* scenario was done to separate the influences of isoprene sinks associated with HO production from ozonelysis of monoterpnes. There are monoculture forested ecosystems that only emit isoprene (Fuentes et al., 1999). The second simulation combined isoprene and monoterpenes (*Mon*), R28 – R34. In this simulation, monoterpenes were represented by a single chemical species whose reactivity ($k_{\mathrm{O_{3,Mono}}} = 1.82 \times 10^{-16}\,cm^3\,molec^{-1}\,s^{-1}$) was calculated as the weighted geometric mean of the composition of monoterpenes observed at the study site (Jardine et al., 2015a). The third simulation (*Pin*) assumed that the emitted monoterpenes had the reactivity of α-pinene ($k_{\mathrm{O_{3,Pin}}} = 8.09 \times 10^{-17}\,cm^3\,molec^{-1}\,s^{-1}$) as assumed in other atmospheric

chemistry models (Emmons et al., 2010). Finally, for the purposes of assessing the importance of chemistry versus transport of monoterpenes, non-reactive tracers were also included in the simulations. These were referred to as passive monoterpenes (Mon_{Pas}), but their emission and deposition were estimated in the same manner as the reactive chemical species.

2.4. Fluxes and budgets of isoprene and monoterpenes

The LES results were analyzed for the canopy region ($0 \leq z \leq h_c$). Average gas mixing ratios within the canopy volume were obtained from Equation (4) by calculating averages over horizontal planes (temporal averages were also obtained over periods of 10 minutes). Resulting averages were vertically integrated to derive the change of gas mixing ratio with time ($\frac{d\langle\tilde{\chi}_j\rangle_{\mathrm{Can}}}{dt}$), given by

$$\frac{d\langle\tilde{\chi}_j\rangle_{\mathrm{Can}}}{dt} = \frac{1}{h_c}\left[-F_j(h_c) + E_{j,\mathrm{Can}} - D_{j,\mathrm{Can}} + C_{j,\mathrm{Can}}\right]. \tag{6}$$

Here $\langle\tilde{\chi}_j\rangle_{\mathrm{Can}} \equiv h_c^{-1}\int_0^{h_c}\langle\tilde{\chi}_j\rangle_{xy}\, dz$ is the mean gas mixing ratio inside the canopy, $\langle\tilde{\chi}_j\rangle_{xy}$ is the horizontally-averaged mixing ratio, $F_j(h_c)$ is the total gas flux at the top of the canopy (including contributions from resolved and SGS fluxes). The hydrocarbon flux at the surface was assumed to be zero. The isoprene surface deposition was prescribed as $V_{\mathrm{dep}} = 2.7\,\mathrm{mm\,s^{-1}}$ (Gordon et al., 2014; Nguyen et al., 2015) and the deposition of monoterpenes was set to zero.

3. Results and Discussion

3.1. Canopy emissions of isoprene and monoterpenes

During the rainy season in the central Amazon, prevailing atmospheric conditions from sunrise to local noontime kept recurring day after day. Afternoons became predominantly cloudy and rainfall events mostly occurred during 14:00 to 16:00 local h (Fuentes et al., 2016; Vilà-Guerau de Arellano et al., 2020). Because the principal goal of this study was to estimate the in-canopy oxidation rates of isoprene and monoterpenes, the numerical model simulations focused on a representative day (14 September 2014) during the start of the rainy season. Sunny conditions dominated the period of the numerical simulations, with maximum incoming solar irradiance reaching nearly 1200 W $\mathrm{m^{-2}}$ around 11:00 h. Clouds appeared around 11:00 h and reduced the incoming sunlight levels during the last hour of simulations (Figure 1a). Air temperature varied from 23 (at 6:30 h) to 32 ^{o}C (at 12:00 h) while wind speed remained below 3.5 m $\mathrm{s^{-1}}$ (Figure 1b, c). Computed emissions of isoprene and monoterpenes increased after sunrise and reached values of 8.0 and 1.5 mg $\mathrm{m^{-2}}$

h^{-1} at 12:00 h (Figure 1d), respectively. Emission rates (Figure 1d) were in good agreement with previously reported canopy-scale fluxes in the central Amazonia region (Rinne et al., 2002; Kuhn et al., 2007). Isoprene emission density profiles changed rapidly with canopy depth (Figure 1e), reaching maximum values of 0.4 mg m^{-3} h^{-1} around 12:00 h at z h_c^{-1} = 0.6 where the greatest amount of active biomass was present and most PAR interception occurred. As emissions of monoterpenes were independent of PAR, the bulk of emissions originated from deeper in the forest canopy (z $h_c^{-1} > 0.4$), with maximum emission density values of 0.075 mg m^{-3} h^{-1} (Figure 1f).

The thermodynamic conditions of the convective ABL exerted control on the vertical distribution of isoprene and monoterpenes. The LES-chemistry coupled model provided high-resolution temporal Z_i variations. Under the assumed atmospheric thermodynamic conditions, simulated Z_i rapidly changed over the course of the morning hours and Z_i values ranged from 200 m at 8:00 h to approximately 760 m at 12:00 h (Figure 2 a). Simulated Z_i values at 11:00 h and 14:00 h were comparable to mixed layer depths of 491 ± 133 m and 813 ± 128 m, respectively, observed 24 km away from the study site during the wet season (Fisch et al., 2004). Additional details on the atmospheric boundary layer thermodynamic evolution as well as turbulence statistics are provided in the the Supplement (Figures S1-S4). Meanwhile, canopy emissions of isoprene and monoterpenes contributed to rapid increases in mixing ratios of the gases in the convective boundary layer. Most of the emitted hydrocarbons remained in the convective boundary layer, with mixing ratios close to zero ppb in the entrainment zone above the mixed layer (Figures 2b, c). Isoprene mixing ratios in the ABL exhibited a high sensitivity to variations in Z_i (Wei et al., 2018), so that even small perturbations in the dynamics of the convective boundary layer considerably impacted the vertical distribution and mixing ratios of isoprene and monoterpenes. While nearly constant θ_v prevailed in the well mixed boundary layer above the canopy (Figure 2a), isoprene (*Iso*, Figure 2b) and monoterpene (*Mon*, Figure 2c) levels revealed strong vertical gradients in response to the source strength of the gases in the canopy, and the ensuing turbulent transport and air chemistry. The cases of *Iso* and *Mon* exhibited greatest gas gradients near the forest canopy and the magnitude of gradients increased with height in the upper ABL in response to the gas transport to the free atmosphere and the downward transfer of air parcels nearly devoid of isoprene and monoterpenes from aloft to the top of the mixed layer. Within the mixed layer, the *Iso* and *Mon* cases showed

relatively invariant gas mixing ratios with altitude due to the effective atmospheric turbulent transport. The appreciable differences estimated between the vertical distribution of *Mon* and Mon_{Pas} (Figure 2d) near the forest canopy resulted due to the higher reactivity associated with the *Mon* case.

Simulated ambient levels of isoprene, monoterpenes, and O_3 were contrasted with observations to ascertain the fidelity of LES outputs. At the canopy top (h_c), during 6:00 to 9:00 h temporal patterns of simulated isoprene (Figure 3a) closely matched observations. Thereafter, estimated levels of isoprene progressively diverged from observations and reached maximum discrepancies around 12:00 h, leading to approximately 30% higher isoprene mixing ratios than observations. Modeled monoterperpene mixing ratios overestimated the observations (Figure 3b). Differences between simulated and observed monotepene levels steadily increased as simulations proceeded, reaching nearly 35% higher monoterpenes mixing ratios than observations (Figures 3b). Previous studies (Alves et al., 2016) also found greater estimated monoterpene mixing ratios than observations, with higher mixing ratios of total monoterpenes estimated during daytime in response to the light-dependent emissions (Rinne et al., 2002; Kuhn et al., 2002; Jardine et al., 2015a), and the likely inadequate representation the actual light-dependent behavior of monoterpene emissions in low light conditions in the morning hours. As demonstrated in previous studies (Kuhn et al., 2007; Alves et al., 2016), emissions of isoprene and monoterpenes were likely overestimated in response to variations in the basal emissions throughout the canopy environment. Also, mixing ratios of isoprene and monoterpenes were sensitive to variations in the values of Z_i ((Wei et al., 2018) so that underestimation of simulated mixing-layer heights in the LES may be responsible for the overestimation of above canopy isoprene and monoterpene mixing ration. Simulated temporal variations of O_3 mixing ratio at the canopy top closely matched observations (Figure 3c), with LES results underpredicting O_3 by an average of 5%. At $zh_c^{-1} = 1.14$, the O_3 levels varied from 12 to 24 ppb over the course of the simulation period (Figure 3c). Once the influences of chemical reactions were integrated for the full canopy, the *Iso*, *Mon*, and *Pin* scenarios produced similar patterns in ambient gas levels at the canopy top (Figure 3).

3.2. Processes controlling canopy budgets of isoprene and monoterpenes

Emissions and turbulent transport dominated the processes controlling the isoprene budget in the rainforest canopy. At midday, isoprene emissions contributed to 80 ppbv h^{-1} whereas turbulent

transport carried 75 ppbv h^{-1} out of the canopy. On average, surface deposition and air chemistry accounted for 1–2% and $< 5\%$ of the total isoprene budget destroyed in the canopy (Figure 4a), respectively. The condensed photochemical mechanism (Table S1) employed to investigate chemical reactions in the canopy did not consider the influences of HO recycling associated with isoprene oxidation (Taraborrelli et al., 2012; Fuchs et al., 2013). The small chemical loss resulted because most of the isoprene was emitted in the forest crown (Figure 1e) where air turbulence became strongest and median air parcel residence times varied from seconds to ten minutes (Gerken et al., 2017). Such time scales were much shorter than the isoprene lifetime of about 1.0 hour due to the HO reaction. In addition, limited isoprene emissions occurred in the lower region of the forest canopy (Figure 1e) where actinic irradiance (Moon et al., 2020) and oxidant levels (Freire et al., 2017) ordinarily remained low to drive isoprene chemical reactions. Similar patterns in the budget terms prevailed for monoterpenes, with emissions and turbulent transport contributing with 8.5 and 7.5 ppbv h^{-1} (Figure 4b), respectively. For the *Mon* case, in-canopy oxidation removed approximately 5–10% of emitted monoterpenes. In contrast, for the *Pin* scenario, reactions destroyed 3–5% of emitted gases due to the lower reactivity (for α–pinene) assumed in the photochemical mechanism (see Figure S5 of the Supplement). Compared to isoprene, the greater chemical loss occurred because emissions of monoterpenes prevailed throughout the canopy (Figure 1f) where air parcels remained long enough to allow chemical reactions to occur and generate HO, thereby producing a positive feedback loop to augment chemical reactions involving HO in the full canopy volume. Previous studies (Makar et al., 1999; Stroud et al., 2005; Fuentes et al., 2007) reported similar results for monoterpenes in temperate forests. Hence, one conclusion is that chemical processing in tropical, dense forests consumes appreciable amounts of monotertpenes (Figure 4b) and needs to be considered in numerical models designed to determine BVOC budgets.

Ozone and HO dominated the oxidation of monoterpenes whereas HO controlled the isoprene chemistry in the forest canopy. Based on the individual terms of the mass budget relationship (6), turbulent transport and surface deposition accounted for 38% and 35% of the O_3 budget (Figure 4c), respectively. These results agreed with earlier findings (Freire et al., 2017). On average, the O_3 sink due to chemical reactions in the canopy represented 5% of the canopy budget. The small chemical O_3 sink (Figure 4c) resulted largely in response to the low NO levels (< 0.5 ppb) and relatively slow rate of O_3 reaction with isoprene ($k_{O_{3,Iso}} = 1.30 \times 10^{-17}$ cm^3 $molec^{-1}$ s^{-1}), which was the dominant

hydrocarbon in the forest canopy (Fuentes et al., 2016). The O_3 plus NO reaction only consumed 0.5 ppb h^{-1} whereas reactions with monoterpenes removed O_3 molecules at the rate of 0.4 ppb h^{-1} (Figure 4d). Trace NO_2 levels (< 0.1 ppb) prevailed in the forest canopy. As a result, the sink for O_3 due to reaction with NO_2 reached nearly 0 ppb h^{-1} (Figure 4d). Sesquiterpenes were not considered in the photochemical mechanism, but such gases could represent a significant sink for O_3 within the canopy due to their rapid ozonelysis (Jardine et al., 2011, 2015a) whose reactivity value could be as high as $k_{O_{3,Caryo}} = 1.16 \times 10^{-14}\,cm^3\,molec^{-1}\,s^{-1}$ for the $\beta-$caryophyllene ($C_{15}H_{24}$) molecule.

In the case of HO, chemical reaction rates nearly balanced the net turbulent (upward and downward) transport, each budget term amounting to absolute values of approximately 350 radicals $cm^{-3}\,s^{-1}$. As expected, the storage term remained close to zero radicals $cm^{-3}\,s^{-1}$ in response to the rapid formation and destruction of HO (Figure 4 e). Individual reactions revealed the salient HO sinks and sources (contributions of select individual reactions were estimated indirectly from the reaction constants and modeled concentrations). For example, the reaction rate of monoterpenes with HO (R28) produced 1.8×10^6 radicals cm^{-3} s^{-1} whereas the reaction rate of isoprene with HO (R9) consumed 3.0×10^6 radicals cm^{-3} s^{-1} (Figure 4 f). The HO source from the ozonolysis of monoterpenes in the rainforest closely agreed with previous estimates of 10^6 radicals $cm^{-3}\,s^{-1}$ (Gerken et al., 2016). The HO formation or consumption rates occurred while averaged mixing ratios of monoterpenes and isoprene reached 1 and 10 ppb, respectively, with prevailing NO levels of < 0.5 ppb in the forest canopy. The abundance of isoprene dominated the HO sink in the upper canopy. Due to the high reactivity of monoterpenes with O_3, the HO source from the reaction of monoterpenes with O_3 (R29) greatly exceeded the HO sink from the reaction of monoterpenes with HO (R28). In the forest canopy, O_3 and monoterpenes had much greater mixing ratios than HO levels and also had greater lifetimes. Therefore, the magnitude of the estimated HO source became less affected by competing reactions than the HO sink from isoprene reactions. This finding highlights the crucial role of monoterpenes in maintaining a photochemically active forest environment through the generation of HO.

3.3. Vertical variability of HO source and sinks in the forest canopy

Source and sink of HO resulting from the oxidation of isoprene and monoterpenes exhibited strong vertical variations in the forest canopy. The LES results showed that HO concentrations

associated with isoprene reaction (R9) increased (i.e., became more negative) with time of day and decreased with canopy depth (Figure 5 a). Maximum HO consumption occurred around 12:00 h when the destruction rate reached -4.0×10^6 radicals $cm^{-3}s^{-1}$ in the upper ($z/h_c >$ 0.85) canopy. At the canopy depth of $z/h_c = 0.25$, the HO destruction rate was 50% lower than the values determined in the forest crown in response to the reduced actinic irradiance flux due to canopy shading, which reduced photochemical production of HO (R1 + R2), and limited isoprene emissions. In contrast, the HO formation rate resulting from oxidation of monoterpenes (*Mon*, *Pin*) increased with time of day and canopy depth (Figure 5 b). Despite the comparatively low ambient O_3 levels in Amazonia ($\overline{[O_3]} \sim 10$ ppb) during the wet season (Dias-Junior et al., 2017), the ozonelysis of monoterpenes (R29) yielded maximum HO formation rates ranging from $+2.0 \times 10^6$ radicals cm^{-3} s^{-1} in the lower canopy to $+1.3 \times 10^6$ radicals cm^{-3} s^{-1} in the forest crown around 12:00 h. Compared to the *Pin* scenario, the *Mon* case contributed to greater HO yield (see the Supplement) due to the higher O_3 reactivity for the assumed average monoterpene ($k_{O_{3,Mono}} = 1.82 \times 10^{-16}$ versus $k_{O_{3,Pin}} = 8.09 \times 10^{-17}$ cm^3 $molec^{-1}$ s^{-1}). The HO formation rates (Figures 5 a, b) were computed while the range of NO levels prevailed < 0.5 ppb. However, as confirmed by previous studies (Rohrer et al., 2014; Vilà-Guerau de Arellano et al., 2011; Wei et al., 2018), HO yields strongly depend on NOx concentrations. As revealed by the fraction of HO production from oxidation of monoterpenes (R28, R29) to HO consumption by isoprene (R9), sources and sinks of HO remained closely in balance at canopy depths $z/h_c < 0.25$ (Figure 5 c). In addition, the absolute ratio of HO destruction rate (involving the isoprene reaction) to the simulated HO concentration ($|Sink_{HO_{Iso}}|/[HO]$), which was a measured of HO reactivity in the canopy, exhibited minor variations with canopy depth. The LES-derived HO reactivity values for isoprene varied from 10 s^{-1} at 08:00 h to 40 s^{-1} at 12:00 h. The computed reactivity values were similar to the daytime quantities of 10–30 s^{-1} observed in an Amazonian rainforest during the dry season (Nölscher et al., 2016). Overall, the oxidation of monoterpenes in the lower forest canopy ($z/h_c < 0.25$) generated enough HO to balance the HO needed to drive the isoprene reaction (Figure 5). Because the Amazon rainforest emits a plethora of reactive sesquiterpenes (not considered in this study) and monoterpenes (Jardine et al., 2015a), the HO production from oxidation of emitted hydrocarbons can be greater than the values (Figures 5) reported in this study. Additionally, HO yields from ozonelysis of monoterpenes and sesquiterpenes can be expected to

greatly vary in response to increases in NOx levels associated with biomass burning and/or regional air pollution (Wei et al., 2019). In the central Amazon, sesquiterpenes (such as β-caryophyllene, α-humulene, α-copaene) can reach mixing ratios of 0.5 ppb in the crown of the rainforest (Jardine et al., 2011).

4. Summary and conclusions

Based on the three posed research questions, several conclusions were derived. First, emissions, turbulent transport, surface deposition, and chemical reactions governed temporal and spatial patterns of isoprene and monoterpenes in and above the rainforest. Despite sufficient active biomass distributed throughout the canopy volume, approximately 85% of isoprene emissions came from the upper ($z/h_c > 0.40$) canopy. Maximum isoprene emission density reached 400 $\mu g\, m^{-3}\, h^{-1}$ at $z/h_c \approx 0.60$ around noontime. In part, the greater emissions in the forest crown occurred because the high leaf area density in the upper canopy intercepted most of the incoming photosynthetically active radiation needed to promote isoprene emissions. In contrast, emissions of monoterpenes occurred throughout the forest canopy in response to the suitable conditions (e.g., temperature) to drive emissions. The greatest emission density of monoterpenes was 75 $\mu g\, m^{-3}\, h^{-1}$ at $z/h_c \approx 0.60$ around noontime. The unusually high emission densities gave rise to maximum ambient levels of isoprene and monoterpenes of 8 and 0.8 ppb, respectively, at $z/h_c = 1.14$. Mixing ratios of isoprene and monoterpenes remained effectively dispersed in the mixed layer but rapidly decreased with altitude in the upper region of the convective boundary layer, attaining mixing ratio values close to zero ppb just above the entrainment zone.

Second, chemical reactions and surface deposition destroyed some isoprene and monoterpenes in the forest canopy. Under the influences of observed ozone (< 25 ppb) and nitric oxide (< 0.5 ppb) levels, isoprene destruction due to the chemical reactions amounted to $< 5\%$ of the canopy emissions. The reaction with the hydroxyl radical dominated the chemical sink of isoprene in the canopy. The small chemical loss resulted because most of the emitted isoprene occurred in the upper canopy where air parcel residence times were substantially shorter than the isoprene lifetime. In addition, while substantial isoprene levels persisted in the forest canopy, the low ozone (directly) and nitric oxide (indirectly) levels limited the isoprene chemical sink. In the case of monoterpenes, chemical reactions destroyed approximately 10% of the total canopy emissions. The ozonelysis of monoter-

penes became the dominant chemical sink in the canopy. Because emissions of monoterpenes took place throughout the canopy and air parcels in the lower canopy had longer residence times, the molecules had greater likelihood to partake in chemical reactions before the gases were exported out of the forest canopy.

Third, concomitant and copious emissions of isoprene and monoterpenes within the tropical forest canopy mixed and interacted with ozone and hydroxyl radical to create a unique chemical environment. While both ozone and hydroxyl radical contributed to the oxidation of isoprene and monoterpenes, their role for in–canopy air chemistry was fundamentally different. Ozone was principally carried from aloft into the canopy through turbulent transport whereas hydroxyl radical was continuously produced, destroyed, and recycled in the rainforest canopy. Decreasing actinic fluxes due to shading in the dense canopy reduced light–dependent hydroxyl radical formation rates in the lower air canopy layers. At the same time, the ozonelysis became the most important chemical sink of monoterpenes and contributed to the formation of hydroxyl radical whose yield reached $\approx 2 \times 10^6\,\mathrm{radicals\,cm^{-3}\,s^{-1}}$. Therefore, in dense forest canopies with co–located emissions of isoprene and monoterpenes, the oxidation of hydrocarbon molecules can produce sufficient hydroxyl radical levels to maintain a photochemically active environment. The degree of photochemical activity in the canopy would substantially depend on the levels of both ozone and nitrogen oxides, and reactivity of emitted hydrocarbon molecules.

Acknowledgments

The authors thank G. Katul for comments and suggestions. The U.S. Department of Energy supported the field studies as part of the GoAmazon 2014/5 project (grant SC0011075). Fundação de Amparo à Pesquisa do Estado de São Paulo (FAPESP) and Fundação de Amparo à Pesquisa do Estado do Amazonas (FAPEAM) funded the Brazilian component of the field studies. The Large scale Biosphere-Atmosphere Experiment in Amazonia (LBA) provided logistic support and made the flux tower and housing unit available to complete the field studies. We thank the support from the LBA central office that operated at INPA. We acknowledge logistical support from the ARM Climate Research Facility. JDF acknowledges support from the National Oceanic and Atmospheric Administration, Educational Partnership Program, U.S. Department of Commerce, under Agreement No. NA16SEC4810006-NCAS-M and the National Science Foundation (Award 2000403). The data needed for reproducing the figures are available from the authors upon request. We thank an anonymous reviewer who provided excellent comments to improve the original manuscript.

References

Alves, E.G., Jardine, K., Tota, J., Jardine, A., Yãnez-Serrano, A.M., Karl, T., Tavares, J., Nelson, B., Gu, D., Stavrakou, T., et al., 2016. Seasonality of isoprenoid emissions from a primary rainforest in central Amazonia. Atmospheric Chemistry and Physics 16, 3903–3925.

Arneth, A., Schurgers, G., Lathiere, J., Duhl, T., Beerling, D., Hewitt, C., Martin, M., Guenther, A., 2011. Global terrestrial isoprene emission models: Sensitivity to variability in climate and vegetation. Atmospheric Chemistry and Physics 11, 8037–8052.

Aschmann, S.M., Arey, J., Atkinson, R., 2002. OH radical formation from the gas-phase reactions of O_3 with a series of terpenes. Atmospheric Environment 36, 4347–4355.

Atkinson, R., 2000. Atmospheric chemistry of VOCs and NO_x. Atmospheric environment 34, 2063–2101.

Atkinson, R., Aschmann, S.M., Arey, J., Shorees, B., 1992. Formation of OH radicals in the gas phase reactions of O_3 with a series of terpenes. Journal of Geophysical Research: Atmospheres 97, 6065–6073.

Barr, J., Fuentes, J., Bottenheim, J., 2003. Radiative forcing of phytogenic aerosols. Journal of Geophysical Research: Atmospheres 108.

Bates, K.H., Jacob, D.J., 2019. A new model mechanism for atmospheric oxidation of isoprene: global effects on oxidants, nitrogen oxides, organic products, and secondary organic aerosol. Atmospheric Chemistry and Physics 19, 9613–9640.

Bou-Zeid, E., Meneveau, C., Parlange, M.B., 2004. Large-eddy simulation of neutral atmospheric boundary layer flow over heterogeneous surfaces: Blending height and effective surface roughness. Water Resour. Res. 40, W02505. doi:10.1029/2003WR002475.

Chamecki, M., Meneveau, C., Parlange, M.B., 2008. A hybrid spectral/finite-volume algorithm for Large-Eddy Simulation of scalars in the atmospheric boundary layer. Boundary Layer Meteorol. 128, 473–484. doi:10.1007/s10546-008-9302-1.

Chamecki, M., Meneveau, C., Parlange, M.B., 2009. Large eddy simulation of pollen transport in the atmospheric boundary layer. J. Aerosol Sci. 40, 241–255. URL: http://www.sciencedirect.com/science/article/pii/S0021850208002024, doi:10.1016/j.jaerosci.2008.11.004.

Dai, Y., Dickinson, R.E., Wang, Y.P., 2004. A two-big-leaf model for canopy temperature, photosynthesis, and stomatal conductance. J. Climate 17, 2281–2299. doi:10.1175/1520-0442(2004)017<2281:ATMFCT>2.0.CO;2.

Dias-Junior, C.Q., Dias, N.L., Fuentes, J.D., Chamecki, M., 2017. Convective storms and non-classical low-level jets during high ozone level episodes in the Amazon region: An ARM/GOAMAZON case study. Atmospheric environment 155, 199–209.

Edburg, S.L., Stock, D., Lamb, B.K., Patton, E.G., 2011. The effect of the vertical source distribution on scalar statistics within and above a forest canopy. Boundary Layer Meteorol. 142, 365–382. doi:10.1007/s10546-011-9686-1.

Edwards, P., Evans, M., Furneaux, K., Hopkins, J., Ingham, T., Jones, C., Lee, J., Lewis, A., Moller, S., Stone, D., et al., 2013. OH reactivity in a South East Asian tropical rainforest during the Oxidant and Particle Photochemical Processes (OP3) project. Atmospheric Chemistry and Physics 13, 9497–9514.

Emmons, L.K., Walters, S., Hess, P.G., Lamarque, J.F., Pfister, G.G., Fillmore, D., Granier, C., Guenther, A., Kinnison, D., Laepple, T., Orlando, J., Tie, X., Tyndall, G., Wiedinmyer, C., Baughcum, S.L., Kloster, S., 2010. Description and evaluation of the Model for Ozone and Related chemical Tracers, version 4 (MOZART-4). Geosci. Model Dev. 3, 43–67. URL: http://www.geosci-model-dev.net/3/43/2010/, doi:10.5194/gmd-3-43-2010.

Finnigan, J., 2000. Turbulence in plant canopies. Annual Review of Fluid Mechanics 32, 519–571.

Fisch, G., Tota, J., Machado, L.a.T., Dias, M.A.F.S., Lyra, R.F.d.F., Nobre, C.A., Dolman, A.J., Gash, J.H.C., 2004. The convective boundary layer over pasture and forest in Amazonia. Theor Appl Climatol 78, 47–59. doi:10.1007/s00704-004-0043-x.

Fitzjarrald, D.R., Moore, K.E., 1990. Mechanisms of nocturnal exchange between the rain forest and the atmosphere. Journal of Geophysical Research: Atmospheres 95, 16839–16850.

Fitzjarrald, D.R., Moore, K.E., Cabral, O.M., Scolar, J., Manzi, A.O., de Abreu Sá, L.D., 1990. Daytime turbulent exchange between the Amazon forest and the atmosphere. Journal of Geophysical Research: Atmospheres 95, 16825–16838.

Foken, T., 2006. 50 years of the Monin–Obukhov similarity theory. Boundary-Layer Meteorology 119, 431–447.

Freire, L., Gerken, T., Ruiz-Plancarte, J., Wei, D., Fuentes, J., Katul, G., Dias, N., Acevedo, O., Chamecki, M., 2017. Turbulent mixing and removal of ozone within an Amazon rainforest canopy. Journal of Geophysical Research: Atmospheres 122, 2791–2811.

Fuchs, H., Hofzumahaus, A., Rohrer, F., Bohn, B., Brauers, T., Dorn, H., Häseler, R., Holland, F., Kaminski, M., Li, X., et al., 2013. Experimental evidence for efficient hydroxyl radical regeneration in isoprene oxidation. Nature Geoscience 6, 1023–1026.

Fuentes, J., Wang, D., Gu, L., 1999. Seasonal variations in isoprene emissions from a boreal aspen forest. Journal of Applied Meteorology 38, 855–869.

Fuentes, J.D., Chamecki, M., Nascimento dos Santos, R.M., Von Randow, C., Stoy, P.C., Katul, G., Fitzjarrald, D., Manzi, A., Gerken, T., Trowbridge, A., et al., 2016. Linking meteorology, turbulence, and air chemistry in the Amazon rain forest. Bulletin of the American Meteorological Society 97, 2329–2342.

Fuentes, J.D., Lerdau, M., Atkinson, R., Baldocchi, D., Bottenheim, J., Ciccioli, P., Lamb, B., Geron, C., Gu, L., Guenther, A., et al., 2000. Biogenic hydrocarbons in the atmospheric boundary layer: a review. Bulletin of the American Meteorological Society 81, 1537–1575.

Fuentes, J.D., Wang, D., Bowling, D.R., Potosnak, M., Monson, R.K., Goliff, W.S., Stockwell, W.R., 2007. Biogenic hydrocarbon chemistry within and above a mixed deciduous forest. Journal of Atmospheric Chemistry 56, 165–185.

Gaskell, P.H., Lau, A.K.C., 1988. Curvature-compensated convective transport: SMART, A new boundedness-preserving transport algorithm. Int. J. Numer. Methods Fluids 8, 617–641. doi:10.1002/fld.1650080602.

Geiger, H., Barnes, I., Bejan, I., Benter, T., Spittler, M., 2003. The tropospheric degradation of isoprene: An updated module for the regional atmospheric chemistry mechanism. Atmos. Environ. 37, 1503–1519. URL: http://www.sciencedirect.com/science/article/pii/S1352231002010476, doi:10.1016/S1352-2310(02)01047-6.

Gerken, T., Chamecki, M., Fuentes, J.D., 2017. Air-parcel residence times within forest canopies. Boundary-Layer Meteorology 165, 29–54.

Gerken, T., Wei, D., Chase, R.J., Fuentes, J.D., Schumacher, C., Machado, L.A., Andreoli, R.V., Chamecki, M., de Souza, R.A.F., Freire, L.S., et al., 2016. Downward transport of ozone rich air and implications for atmospheric chemistry in the Aamazon rainforest. Atmospheric Environment 124, 64–76.

Gordon, M., Vlasenko, A., Staebler, R.M., Stroud, C., Makar, P.A., Liggio, J., Li, S.M., Brown, S., 2014. Uptake and emission of VOCs near ground level below a mixed forest at Borden, Ontario. Atmos. Chem. Phys. 14, 9087–9097. URL: http://www.atmos-chem-phys.net/14/9087/2014/, doi:10.5194/acp-14-9087-2014.

Gu, L., 1999. Modeling biophysical exchanges and micro-meteorology in soil-vegetation-atmosphere continuum: Results from a two-story boreal aspen forest. PhD Dissertation. University of Virginia. Charlottesville, Virginia, United States.

Guenther, A., Karl, T., Harley, P., Wiedinmyer, C., Palmer, P.I., Geron, C., 2006. Estimates of global terrestrial isoprene emissions using MEGAN (Model of Emissions of Gases and Aerosols from Nature). Atmos. Chem. Phys. 6, 3181–3210. URL: http://www.atmos-chem-phys.net/6/3181/2006/, doi:10.5194/acp-6-3181-2006.

Guenther, A.B., Jiang, X., Heald, C.L., Sakulyanontvittaya, T., Duhl, T., Emmons, L.K., Wang, X., 2012. The Model of Emissions of Gases and Aerosols from Nature version 2.1 (MEGAN2.1): An extended and updated framework for modeling biogenic emissions. Geosci. Model Dev. 5, 1471–1492. URL: http://www.geosci-model-dev.net/5/1471/2012/gmd-5-1471-2012.html, doi:10.5194/gmd-5-1471-2012.

Herrmann, F., Winterhalter, R., Moortgat, G.K., Williams, J., 2010. Hydroxyl radical (OH) yields

549 from the ozonolysis of both double bonds for five monoterpenes. Atmospheric Environment 44,
550 3458–3464.

551 Heus, T., van Heerwaarden, C.C., Jonker, H.J.J., Pier Siebesma, A., Axelsen, S., van den Dries,
552 K., Geoffroy, O., Moene, A.F., Pino, D., de Roode, S.R., Vilà-Guerau de Arellano, J., 2010.
553 Formulation of the Dutch Atmospheric Large-Eddy Simulation (DALES) and overview of its
554 applications. Geosci. Model Dev. 3, 415–444. URL: http://www.geosci-model-dev.net/3/
555 415/2010/, doi:10.5194/gmd-3-415-2010.

556 Jardine, A.B., Jardine, K.J., Fuentes, J.D., Martin, S.T., Martins, G., Durgante, F., Carneiro, V.,
557 Higuchi, N., Manzi, A.O., Chambers, J.Q., 2015a. Highly reactive light-dependent monoterpenes
558 in the Amazon. Geophysical Research Letters 42, 1576–1583.

559 Jardine, K.J., Chambers, J.Q., Holm, J., Jardine, A.B., Fontes, C.G., Zorzanelli, R.F., Meyers,
560 K.T., De Souza, V.F., Garcia, S., Gimenez, B.O., et al., 2015b. Green leaf volatile emissions
561 during high temperature and drought stress in a central Amazon rainforest. Plants 4, 678–690.

562 Jardine, K.J., Yañez Serrano, A., Arneth, A., Abrell, L., Jardine, A., Van Haren, J., Artaxo,
563 P., Rizzo, L.V., Ishida, F.Y., Karl, T., et al., 2011. Within-canopy sesquiterpene ozonolysis in
564 Amazonia. Journal of Geophysical Research: Atmospheres 116.

565 Karl, T., Guenther, A., Yokelson, R.J., Greenberg, J., Potosnak, M., Blake, D.R., Artaxo, P., 2007.
566 The tropical forest and fire emissions experiment: Emission, chemistry, and transport of biogenic
567 volatile organic compounds in the lower atmosphere over Amazonia. Journal of Geophysical
568 Research: Atmospheres 112, D18302. doi:10.1029/2007JD008539.

569 Khan, B., Banzhaf, S., Chan, E.C., Forkel, R., Kanani-Sühring, F., Ketelsen, K., Kurppa, M.,
570 Maronga, B., Mauder, M., Raasch, S., et al., 2021. Development of an atmospheric chemistry
571 model coupled to the PALM model system 6.0: Implementation and first applications. Geosci-
572 entific Model Development 14, 1171–1193.

573 Kruijt, B., Malhi, Y., Lloyd, J., Norbre, A., Miranda, A., Pereira, M.G., Culf, A., Grace, J.,
574 2000. Turbulence statistics above and within two Amazon rain forest canopies. Boundary-Layer
575 Meteorology 94, 297–331.

576 Kuhn, U., Andreae, M.O., Ammann, C., Araújo, A., Brancaleoni, E., Ciccioli, P., Dindorf, T.,
577 Frattoni, M., Gatti, L.V., Ganzeveld, L., et al., 2007. Isoprene and monoterpene fluxes from
578 central Amazonian rainforest inferred from tower-based and airborne measurements, and impli-
579 cations on the atmospheric chemistry and the local carbon budget. Atmospheric Chemistry and
580 Physics 7, 2855–2879.

581 Kuhn, U., Rottenberger, S., Biesenthal, T., Wolf, A., Schebeske, G., Ciccioli, P., Brancaleoni,
582 E., Frattoni, M., Tavares, T., Kesselmeier, J., 2002. Isoprene and monoterpene emissions of
583 amazonian tree species during the wet season: Direct and indirect investigations on controlling
584 environmental functions. Journal of Geophysical Research: Atmospheres 107, LBA–38.

585 Lelieveld, J., Butler, T., Crowley, J., Dillon, T., Fischer, H., Ganzeveld, L., Harder, H., Lawrence,
586 M., Martinez, M., Taraborrelli, D., et al., 2008. Atmospheric oxidation capacity sustained by a
587 tropical forest. Nature 452, 737–740.

588 Liu, Y., Brito, J., Dorris, M.R., Rivera-Rios, J.C., Seco, R., Bates, K.H., Artaxo, P., Duvoisin,
589 S., Keutsch, F.N., Kim, S., et al., 2016. Isoprene photochemistry over the Amazon rainforest.
590 Proceedings of the National Academy of Sciences 113, 6125–6130.

591 Liu, Y., Seco, R., Kim, S., Guenther, A.B., Goldstein, A.H., Keutsch, F.N., Springston, S.R.,
592 Watson, T.B., Artaxo, P., Souza, R.A., et al., 2018. Isoprene photo-oxidation products quantify
593 the effect of pollution on hydroxyl radicals over Amazonia. Science Advances 4, eaar2547.

594 Makar, P.A., Fuentes, J.D., Wang, D., Staebler, R.M., Wiebe, H.A., 1999. Chemical processing of
595 biogenic hydrocarbons within and above a temperate deciduous forest. Journal of Geophysical
596 Research: Atmospheres 104, 3581–3603.

597 Marques Filho, A.d.O., Dallarosa, R.G., Pacheco, V.B., 2005. Radiação solar e distribuição vertical
598 de área foliar em floresta – Reserva Biológica do Cuieiras – ZF2, Manaus. Acta Amazonica 35,
599 427–436.

600 McWilliam, A.L.C., Roberts, J.M., Cabral, O.M.R., Leitao, M.V.B.R., de Costa, A.C.L., Maitelli,
601 G.T., Zamparoni, C.A.G.P., 1993. Leaf area index and above-ground biomass of terra firme rain
602 forest and adjacent clearings in Amazonia. Funct. Ecol. 7, 310–317. doi:10.2307/2390210.

603 Moon, Z., Fuentes, J.D., Staebler, R.M., 2020. Impacts of spectrally resolved irradiance on pho-
604 tolysis frequency calculations within a forest canopy. Agricultural and Forest Meteorology 291,
605 108012.

606 Nguyen, T.B., Crounse, J.D., Teng, A.P., Clair, J.M.S., Paulot, F., Wolfe, G.M., Wennberg, P.O.,
607 2015. Rapid deposition of oxidized biogenic compounds to a temperate forest. Proceedings of
608 the National Academy of Sciences 112, E392–E401.

609 Nölscher, A.C., Yañez-Serrano, A.M., Wolff, S., de Araujo, A.C., Lavrič, J.V., Kesselmeier, J.,
610 Williams, J., 2016. Unexpected seasonality in quantity and composition of Amazon rainforest
611 air reactivity. Nat. Commun. 7, 10383. URL: http://www.nature.com/ncomms/2016/160122/
612 ncomms10383/full/ncomms10383.html, doi:10.1038/ncomms10383.

613 Nölscher, A.C., Yáñez-Serrano, A.M., Wolff, S., De Araujo, A.C., Lavrič, J., Kesselmeier, J.,
614 Williams, J., 2016. Unexpected seasonality in quantity and composition of Amazon rainforest
615 air reactivity. Nature communications 7, 1–12.

616 Ouwersloot, H.G., de Arellano, J.V.G., H. van Stratum, B.J., Krol, M.C., Lelieveld, J., 2013. Quan-
617 tifying the transport of subcloud layer reactants by shallow cumulus clouds over the Amazon.
618 Journal of Geophysical Research: Atmospheres 118, 13041–13059. doi:10.1002/2013JD020431.

619 Pan, Y., Chamecki, M., Isard, S.A., 2014. Large-eddy simulation of turbulence and particle
620 dispersion inside the canopy roughness sublayer. J. Fluid Mech. 753, 499–534. URL: http:
621 //journals.cambridge.org/article_S0022112014003796, doi:10.1017/jfm.2014.379.

622 Patton, E.G., Davis, K.J., Barth, M.C., Sullivan, P.P., 2001. Decaying scalars emitted by a
623 forest canopy: A numerical study. Boundary Layer Meteorol. 100, 91–129. doi:10.1023/A:
624 1019223515444.

625 Patton, E.G., Sullivan, P.P., Shaw, R.H., Finnigan, J.J., Weil, J.C., 2016. Atmospheric stability
626 influences on coupled boundary layer and canopy turbulence. Journal of the Atmospheric Sciences
627 73, 1621–1647.

628 Peyret, R., Taylor, T.D., 2012. Computational methods for fluid flow. Springer Science & Business
629 Media.

Pfannerstill, E.Y., Reijrink, N.G., Edtbauer, A., Ringsdorf, A., Zannoni, N., Araújo, A., Ditas, F., Holanda, B.A., Sá, M.O., Tsokankunku, A., et al., 2021. Total OH reactivity over the Amazon rainforest: variability with temperature, wind, rain, altitude, time of day, season, and an overall budget closure. Atmospheric Chemistry and Physics 21, 6231–6256.

Pöschl, U., Martin, S., Sinha, B., Chen, Q., Gunthe, S., Huffman, J., Borrmann, S., Farmer, D., Garland, R., Helas, G., et al., 2010. Rainforest aerosols as biogenic nuclei of clouds and precipitation in the Amazon. Science 329, 1513–1516.

Pöschl, U., Von Kuhlmann, R., Poisson, N., Crutzen, P.J., 2000. Development and intercomparison of condensed isoprene oxidation mechanisms for global atmospheric modeling. Journal of Atmospheric Chemistry 37, 29–52.

Raupach, M.R., Finnigan, J.J., Brunet, Y., 1996. Coherent eddies and turbulence in vegetation canopies: The mixing-layer analogy, in: Boundary-layer meteorology 25th anniversary volume, 1970–1995. Springer, pp. 351–382.

Rinne, H., Guenther, A., Greenberg, J., Harley, P., 2002. Isoprene and monoterpene fluxes measured above amazonian rainforest and their dependence on light and temperature. Atmospheric Environment 36, 2421–2426.

Rinne, J., Markkanen, T., Ruuskanen, T., Petäjä, T., Keronen, P., Tang, M., Crowley, J., Rannik, Ü., Vesala, T., 2012. Effect of chemical degradation on fluxes of reactive compounds–a study with a stochastic lagrangian transport model. Atmospheric chemistry and physics 12, 4843–4854.

Rohrer, F., Lu, K., Hofzumahaus, A., Bohn, B., Brauers, T., Chang, C.C., Fuchs, H., Häseler, R., Holland, F., Hu, M., et al., 2014. Maximum efficiency in the hydroxyl-radical-based self-cleansing of the troposphere. Nature Geoscience 7, 559–563.

Santos, D.M., Acevedo, O.C., Chamecki, M., Fuentes, J.D., Gerken, T., Stoy, P.C., 2016. Temporal scales of the nocturnal flow within and above a forest canopy in Amazonia. Boundary-layer meteorology 161, 73–98.

Schwantes, R.H., Emmons, L.K., Orlando, J.J., Barth, M.C., Tyndall, G.S., Hall, S.R., Ullmann, K., Clair, J.M.S., Blake, D.R., Wisthaler, A., et al., 2020. Comprehensive isoprene and terpene

gas-phase chemistry improves simulated surface ozone in the southeastern us. Atmospheric Chemistry and Physics 20, 3739–3776.

Sellers, P.J., 1985. Canopy reflectance, photosynthesis and transpiration. Int. J. Remote Sens. 6, 1335–1372. doi:10.1080/01431168508948283.

Shaw, R.H., Schumann, U., 1992. Large-eddy simulation of turbulent flow above and within a forest. Boundary Layer Meteorol. 61, 47–64. doi:10.1007/BF02033994.

Sindelarova, K., Granier, C., Bouarar, I., Guenther, A., Tilmes, S., Stavrakou, T., Müller, J.F., Kuhn, U., Stefani, P., Knorr, W., 2014. Global data set of biogenic VOC emissions calculated by the MEGAN model over the last 30 years. Atmospheric Chemistry and Physics 14, 9317–9341.

Strong, C., Fuentes, J., Baldocchi, D., 2004. Reactive hydrocarbon flux footprints during canopy senescence. Agricultural and Forest Meteorology 127, 159–173.

Stroud, C., Makar, P., Guenther, A., Geron, C., Turnipseed, A., Nemitz, E., Baker, B., Potosnak, M., Fuentes, J., 2005. Role of canopy–scale photochemistry in modifying biogenic–atmosphere exchange of reactive terpene species: Results from the CELTIC field study. Journal of Geophysical Research: Atmospheres 110, 1–14.

Su, L., Patton, E.G., Vilà-Guerau de Arellano, J., Guenther, A.B., Kaser, L., Yuan, B., Xiong, F., Shepson, P.B., Zhang, L., Miller, D.O., Brune, W.H., Baumann, K., Edgerton, E., Weinheimer, A., Misztal, P.K., Park, J.H., Goldstein, A.H., Skog, K.M., Keutsch, F.N., Mak, J.E., 2016. Understanding isoprene photooxidation using observations and modeling over a subtropical forest in the southeastern US. Atmos. Chem. Phys. 16, 7725–7741. URL: http://www.atmos-chem-phys.net/16/7725/2016/, doi:10.5194/acp-16-7725-2016.

Taraborrelli, D., Lawrence, M., Crowley, J., Dillon, T., Gromov, S., Groß, C., Vereecken, L., Lelieveld, J., 2012. Hydroxyl radical buffered by isoprene oxidation over tropical forests. Nature Geoscience 5, 190–193.

Tota, J., Roy Fitzjarrald, D., da Silva Dias, M.A., 2012. Amazon rainforest exchange of carbon and subcanopy air flow: Manaus LBA site—A complex terrain condition. The Scientific World Journal 2012.

684 Van Stratum, B., Vilà-Guerau de Arellano, J., Ouwersloot, H., Van Den Dries, K., Van Laar, T.,
685 Martinez, M., Lelieveld, J., Diesch, J.M., Drewnick, F., Fischer, H., et al., 2012. Case study
686 of the diurnal variability of chemically active species with respect to boundary layer dynamics
687 during domino. Atmospheric Chemistry and Physics 12, 5329–5341.

688 Verwer, J., Simpson, D., 1995. Explicit methods for stiff ODEs from atmospheric chemistry. Applied
689 Numerical Mathematics 18, 413–430. URL: http://linkinghub.elsevier.com/retrieve/pii/
690 0168927495000686, doi:10.1016/0168-9274(95)00068-6.

691 Verwer, J.G., 1994. Gauss–Seidel iteration for stiff ODES from chemical kinetics. SIAM J. Sci.
692 Comput. 15, 1243–1250. doi:10.1137/0915076.

693 Vilà-Guerau de Arellano, J., 2015. Atmospheric boundary layer: Integrating air chemistry and
694 land interactions. Cambridge University Press, New York, NY.

695 Vilà-Guerau de Arellano, J., Patton, E.G., Karl, T., van den Dries, K., Barth, M.C., Orlando,
696 J.J., 2011. The role of boundary layer dynamics on the diurnal evolution of isoprene and
697 the hydroxyl radical over tropical forests. Journal of Geophysical Research: Atmospheres 116,
698 D07304. doi:10.1029/2010JD014857.

699 Vilà-Guerau de Arellano, J., Wang, X., Pedruzo-Bagazgoitia, X., Sikma, M., Agustí-Panareda, A.,
700 Boussetta, S., Balsamo, G., Machado, L., Biscaro, T., Gentine, P., et al., 2020. Interactions
701 between the amazonian rainforest and cumuli clouds: A large-eddy simulation, high-resolution
702 ecmwf, and observational intercomparison study. Journal of Advances in Modeling Earth Systems
703 12, e2019MS001828.

704 Wei, D., Fuentes, J.D., Gerken, T., Chamecki, M., Trowbridge, A.M., Stoy, P.C., Katul, G.G.,
705 Fisch, G., Acevedo, O., Manzi, A., et al., 2018. Environmental and biological controls on seasonal
706 patterns of isoprene above a rain forest in central Amazonia. Agricultural and Forest Meteorology
707 256, 391–406.

708 Wei, D., Fuentes, J.D., Gerken, T., Trowbridge, A.M., Stoy, P.C., Chamecki, M., 2019. Influences
709 of nitrogen oxides and isoprene on ozone-temperature relationships in the Amazon rain forest.
710 Atmospheric Environment 206, 280–292.

Whalley, L., Edwards, P., Furneaux, K., Goddard, A., Ingham, T., Evans, M., Stone, D., Hopkins, J., Jones, C.E., Karunaharan, A., et al., 2011. Quantifying the magnitude of a missing hydroxyl radical source in a tropical rainforest. Atmospheric Chemistry and Physics 11, 7223–7233.

Wolfe, G.M., Thornton, J.A., 2011. The Chemistry of Atmosphere-Forest Exchange (CAFE) Model – Part 1: Model description and characterization. Atmos. Chem. Phys. 11, 77–101. URL: http://www.atmos-chem-phys.net/11/77/2011/, doi:10.5194/acp-11-77-2011.

Yáñez-Serrano, A.M., Nölscher, A.C., Bourtsoukidis, E., Gomes Alves, E., Ganzeveld, L., Bonn, B., Wolff, S., Sa, M., Yamasoe, M., Williams, J., et al., 2018. Monoterpene chemical speciation in a tropical rainforest: Variation with season, height, and time of dayat the Amazon tall tower observatory (ATTO). Atmospheric Chemistry and Physics 18, 3403–3418.

Figure captions

Figure 1. a) Incoming solar radiation, b) air temperature, c) wind speed, d) integrated emissions of isoprene and monoterpenes, e) isoprene emission density, and f) monoterpene emission density from 6:00 h to 12:00 h (yellow to dark red) on 14 September 2014. Shaded circles represent select times when data are plotted.

Figure 2. Horizontally averaged profiles of instantaneous a) virtual potential temperature (θ_v) in degrees Kelvin (K) and mixing ratios in ppb of b) isoprene, c) monoterpenes (*Mon*), and d) passive monoterpenes (*Mon*) at 8:00 (black), 10:00 (blue), and 12:00 h (red) on 14 September 2014.

Figure 3. Simulated and observed gas mixing ratios in ppb at $\mathrm{zh}_c^{-1} = 1.14$ of a) isoprene (the *Iso* case indicates only isoprene chemistry, *Mon* means that the chemistry of monoterpenes was added to the isoprene chemistry, *Pin* means the chemistry of α–pinene was added to the isoprene chemistry), b) monoterpenes (*Mon* indicates that the chemistry of monoterpes was combined with isoprene chemistry, *Pin* means the chemistry of α–pinene was added to the isoprene chemistry), and c) ozone for cases *Iso*, *Mon*, and *Pin* on 14 September 2014. Shaded circles represent select times when data are plotted.

Figure 4. Computed budgets of gases at the canopy top. a) Terms in the canopy budget for a) isoprene and b) monoterpenes (*Mon* case). Budget terms include air chemistry (R_{Can}), flux across canopy top ($\mathrm{F}(\mathrm{h}_c)$), change in gas storage ($\mathrm{d}< \chi >/\mathrm{dt}$), canopy emission ($\mathrm{E}_{Can}$), and surface deposition (D_{Can}), which was calculated as the residual of the other terms. Positive values indicate accumulation in the control volume. c) Terms (air chemistry, transport, storage, and surface deposition) of the ozone canopy budget. d) Rates of ozone destruction due to reactions with nitric oxide (NO), nitrogen dioxide (NO_2), and mmonoterpenes (Mon). e) Terms (air chemistry, transport, and storage) of the hydroxyl radical budget. f) Rates of hydroxyl radical destruction or formation due to reactions with isoprene, monoterpenes, and ozonolysis of monoterpenes on 14 September 2014. Shaded circles represent select times when data are plotted.

Figure 5. a) Vertical variation of hydroxyl radical sink due to reaction with isoprene ($\text{Sink}_{HO,Isop}$) and b) source of hydroxyl radical due to rozonolysis of monoterpenes ($\text{Source}_{HO,Mon}$). c) Comparison of source and sink strength of hydroxyl radical as a function of canopy depth. d) The absolute ratio of hydroxyl radical sink due to reaction with isoprene to average ambient hydroxyl radical concentration as a function of canopy depth for 08:00, 10:00, and 12:00 hours on 14 September 2014. Shaded circles represent select heights where data are plotted.

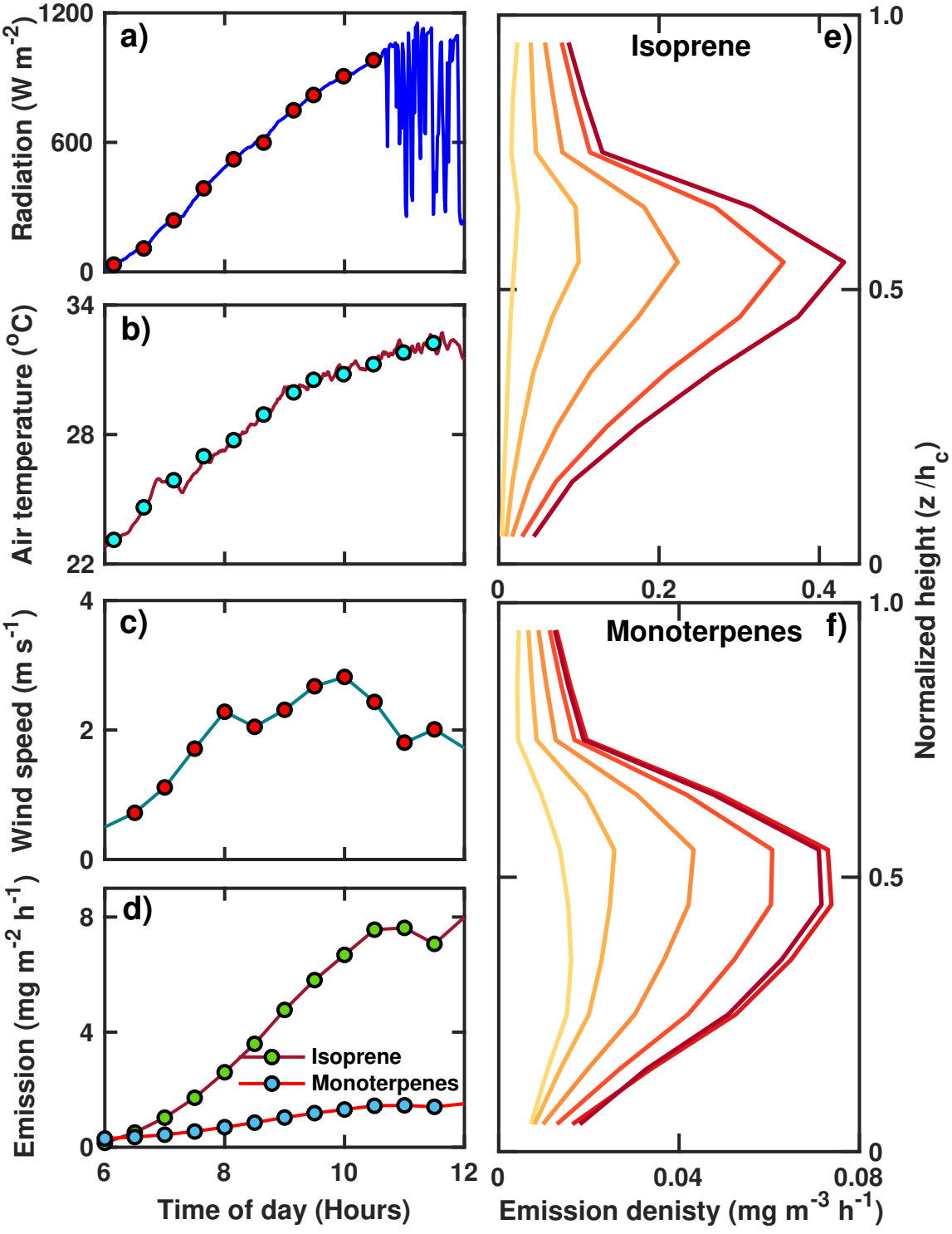
a)
b)
c)
d)
e)
f)
Radiation (W m-2)
Air temperature (°C)
Wind speed (m s-1)
Emission (mg m-2 h-1)
Isoprene
Monoterpenes
Time of day (Hours)
Emission denisty (mg m-3 h-1)
Normalized height (z /hc)
1200
600
0
34
28
22
4
2
0
8
4
0
6
8
10
12
0.2
0.4
0.04
0.08
1.0
0.5

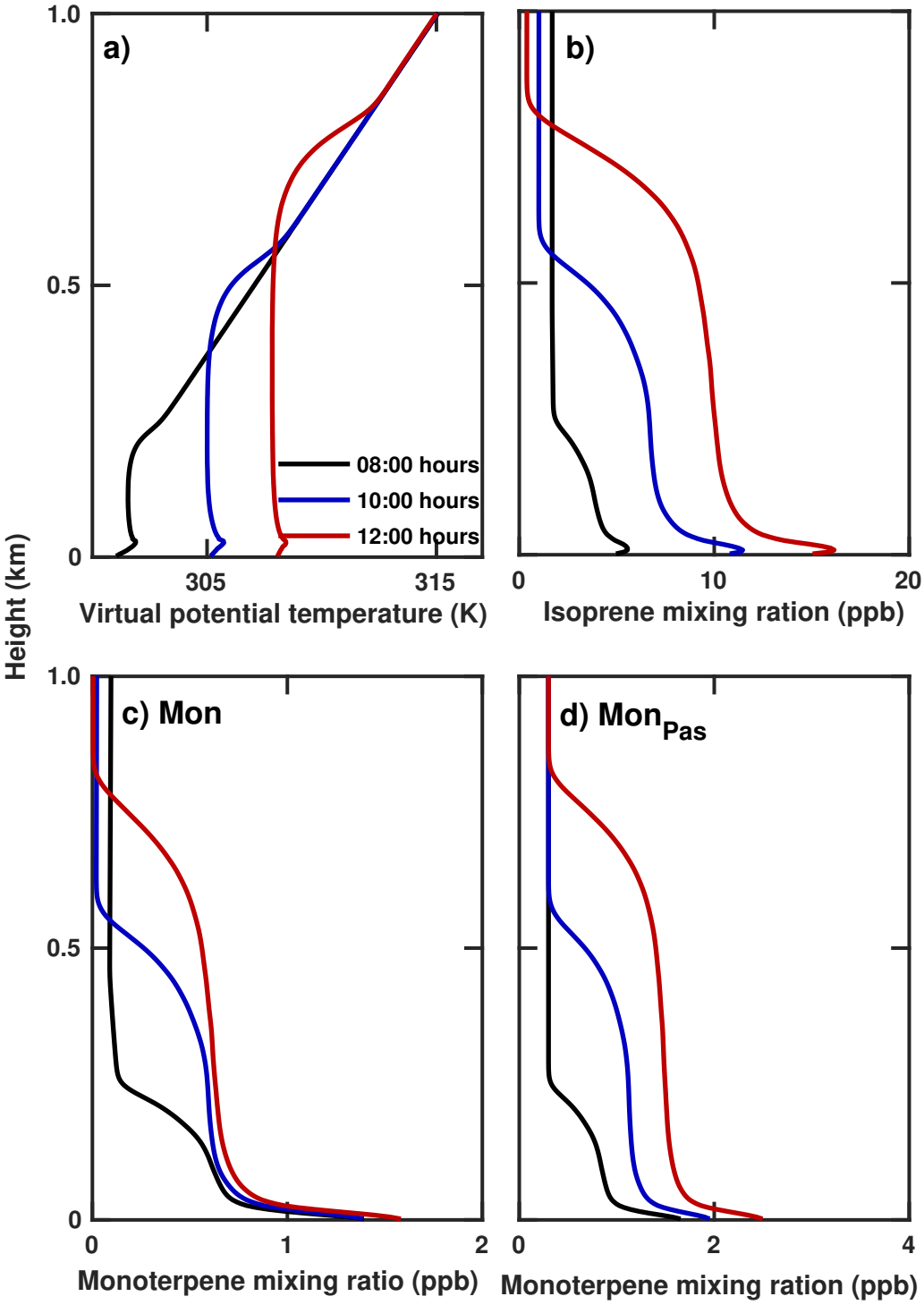
a)
b)
c) Mon
d) Mon$_{Pas}$
Height (km)
1.0
0.5
0
305
315
Virtual potential temperature (K)
08:00 hours
10:00 hours
12:00 hours
0
10
20
Isoprene mixing ration (ppb)
0
1
2
Monoterpene mixing ratio (ppb)
0
2
4
Monoterpene mixing ration (ppb)

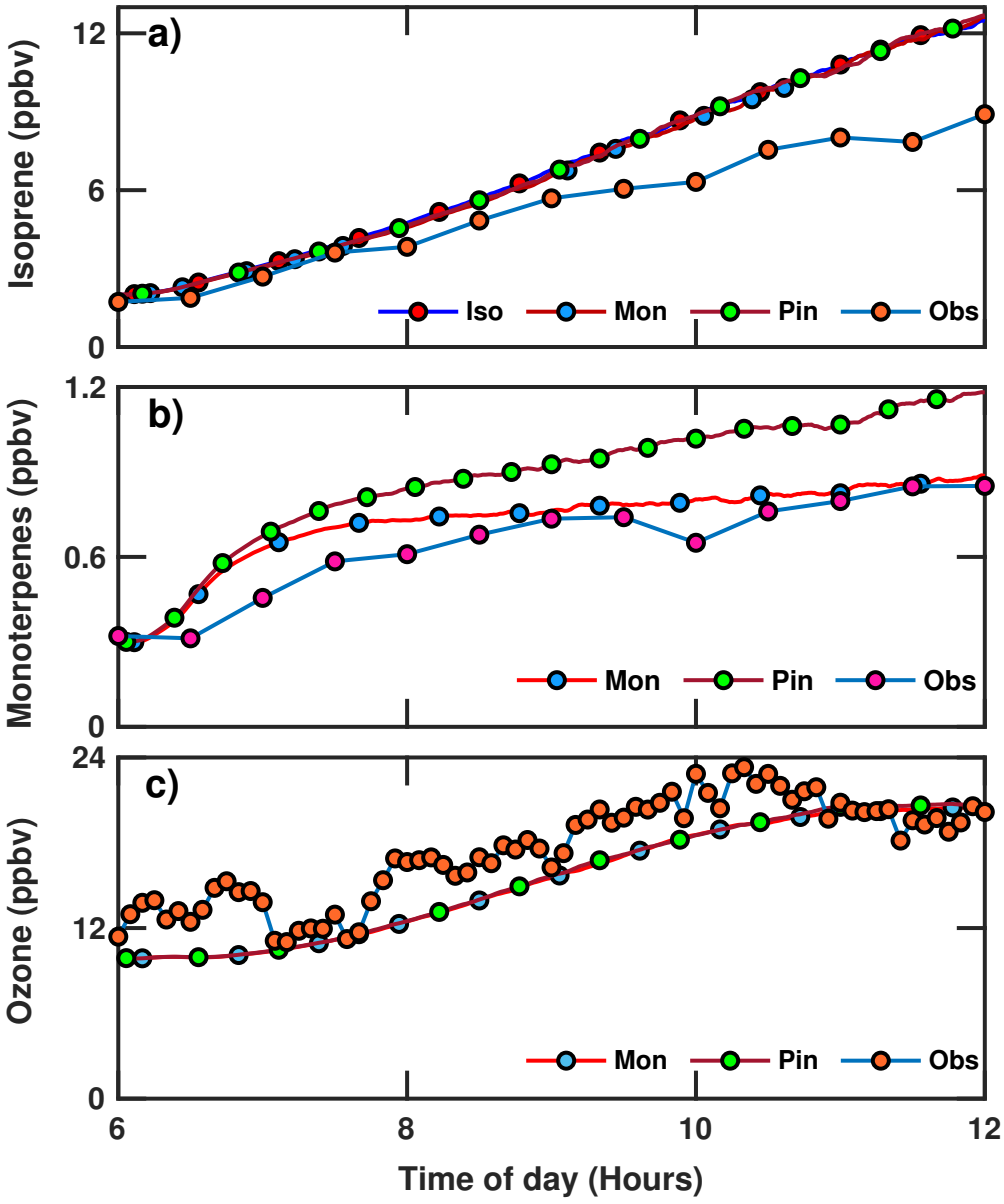
a)
b)
c)
Isoprene (ppbv)
Monoterpenes (ppbv)
Ozone (ppbv)
Iso
Mon
Pin
Obs
Time of day (Hours)
0
6
12
0.6
1.2
8
10
24

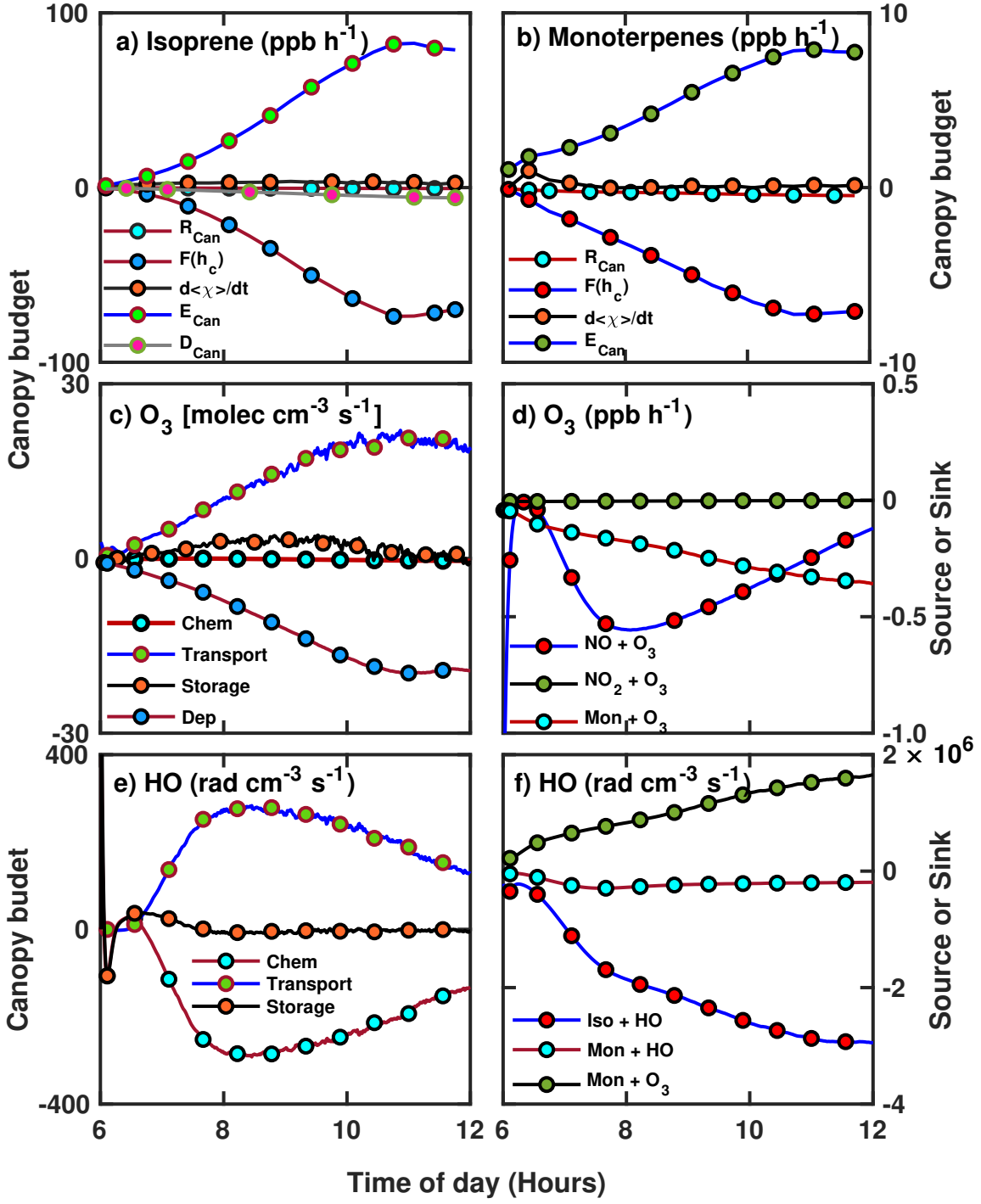
a) Isoprene (ppb h-1)
b) Monoterpenes (ppb h-1)
c) O3 [molec cm-3 s-1]
d) O3 (ppb h-1)
e) HO (rad cm-3 s-1)
f) HO (rad cm-3 s-1)
RCan
F(hc)
d<χ>/dt
ECan
DCan
Chem
Transport
Storage
Dep
NO + O3
NO2 + O3
Mon + O3
Iso + HO
Mon + HO
Canopy budget
Canopy budet
Source or Sink
2 × 10^6
Time of day (Hours)

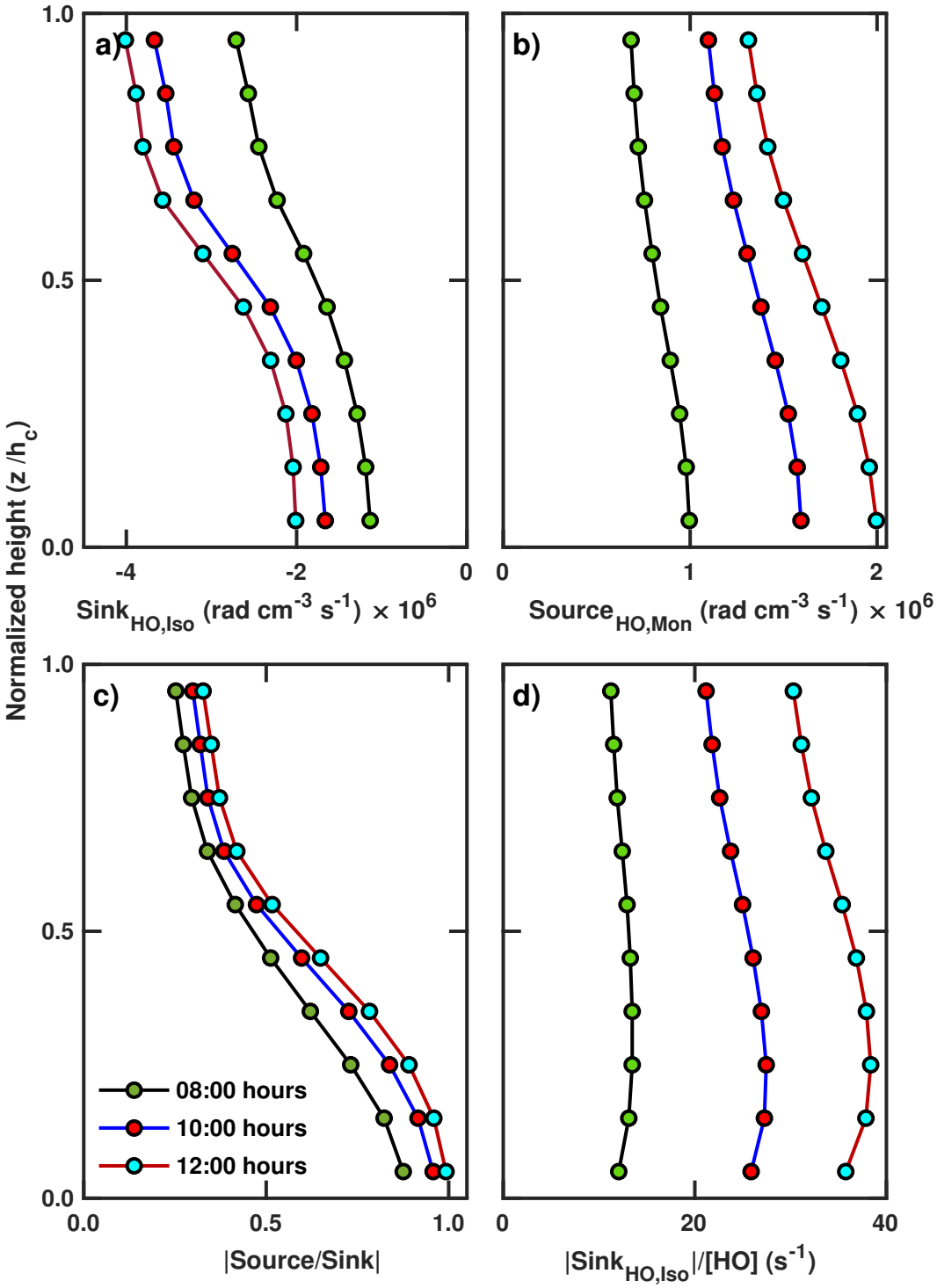
a)
b)
c)
d)
Normalized height (z /h$_c$)
Sink$_{HO,Iso}$ (rad cm^{-3} s^{-1}) × 10^6
Source$_{HO,Mon}$ (rad cm^{-3} s^{-1}) × 10^6
|Source/Sink|
|Sink$_{HO,Iso}$|/[HO] (s^{-1})
08:00 hours
10:00 hours
12:00 hours
1.0
0.5
0.0
-4
-2
0
1
2
20
40

Table 1: Data used to initialize the vertical profiles in the LES domain

Variable	Height	Value	Unit
θ_v	$z \leq 50$	299.1	K
$\Delta\theta_v/\Delta z$	$50\,\mathrm{m} < z \leq 150\,\mathrm{m}$	0.024	$\mathrm{K\,m^{-1}}$
$\Delta\theta_v/\Delta z$	$z > 150\,\mathrm{m}$	0.016	$\mathrm{K\,m^{-1}}$
q	$z \leq 150$	17.0	$\mathrm{g\,kg^{-1}}$
	$z > 150$	13.0	$\mathrm{g\,kg^{-1}}$
O_3	$z \leq 450\,\mathrm{m}$	$8 + 0.056\,\mathrm{ppb\,m^{-1}}\,z$	ppb
	$z > 450\,\mathrm{m}$	33.1	ppb
NO	$z \leq 150\,\mathrm{m}$	0.1	ppb
NO_2		0.1	ppb
CH_4		1724.0	ppb

Supplement

The purpose of this supplement is to provide the details of the photochemical mechanism (see Table S1) included in the updated LES and include additional figures showing the LES results for air turbulence and kinematic heat fluxes in and above the forest canopy.

Table S1: Chemical reaction scheme used in the LES with reactions and their respective rate constants

Number	Reaction	Reaction rate constant[a]
R1	$O_3 + h\nu \rightarrow O(1D) + (O_2)$[b]	$3.83 \cdot 10^{-5} \cdot e^{\frac{-0.575}{\chi}}$
R2	$O(1D) + H_2O \rightarrow 2HO$	$1.63 \cdot 10^{-10} \cdot e^{\frac{60}{T}}$
R3	$O(1D) + (N_2) + (O_2) \rightarrow O_3 + (N_2)$	$2.15 \cdot 10^{-11} \cdot e^{\frac{110}{T}}$
R4	$O(1D) + (O_2) \rightarrow O_3$	$3.30 \cdot 10^{-11} \cdot e^{\frac{55}{T}}$
R5	$NO_2 + h\nu \rightarrow NO + O_3$	$1.67 \cdot 10^{-2} \cdot e^{\frac{-0.575}{\chi}}$
R6	$CH_2O + h\nu \rightarrow HO_2$	$5.88 \cdot 10^{-5} \cdot e^{\frac{-0.575}{\chi}}$
R7	$HO + CO \rightarrow HO_2 + (CO_2)$	$2.40 \cdot 10^{-13}$
R8	$HO + CH_4 \rightarrow CHO_2$	$2.45 \cdot 10^{-12} \cdot e^{\frac{-1775}{T}}$
R9	$HO + ISO \rightarrow RO_2$	$1.00 \cdot 10^{-10}$
R10	$HO + MVK \rightarrow HO_2 + CH_2O$	$2.40 \cdot 10^{-11}$
R11	$HO + HO_2 \rightarrow (H_2O) + (O_2)$	$4.80 \cdot 10^{-11} \cdot e^{\frac{250}{T}}$
R12	$HO + H_2O_2 \rightarrow 2(H_2O)$	$2.90 \cdot 10^{-12} \cdot e^{\frac{-160}{T}}$
R13	$HO_2 + NO \rightarrow HO + NO_2$	$3.50 \cdot 10^{-12} \cdot e^{\frac{250}{T}}$
R14	$CH_3O_2 + NO \rightarrow HO_2 + NO_2 + CH_2O$	$2.80 \cdot 10^{-12} \cdot e^{\frac{300}{T}}$
R15	$RO_2 + NO \rightarrow HO_2 + NO_2 + MVK + CH_2O$	$2.43 \cdot 10^{-12}$
R16	$HO + CH_2O \rightarrow HO_2$	$5.50 \cdot 10^{-12} \cdot e^{\frac{125}{T}}$
R17	$2HO_2 \rightarrow H_2O_2 + (O_2)$	(Vilà-Guerau de Arellano, 2015)
R18	$CH_3O_2 + HO_2 \rightarrow PRODUC$	$4.10 \cdot 10^{-13}$
R19	$RO_2 + HO_2 \rightarrow PRODUC$	$1.50 \cdot 10^{-11}$
R20	$HO + NO_2 \rightarrow HNO_3$	$3.50 \cdot 10^{-12} \cdot e^{\frac{-340}{T}}$
R21	$NO + O_3 \rightarrow NO_2 + (O_2)$	$3.00 \cdot 10^{-12} \cdot e^{\frac{-1500}{T}}$
R22	$NO + NO_3 \rightarrow 2NO_2$	$1.80 \cdot 10^{-11} \cdot e^{\frac{110}{T}}$
R23	$NO_2 + O_3 \rightarrow NO_3 + (O_2)$	$1.40 \cdot 10^{-13} \cdot e^{\frac{-2470}{T}}$
R24	$NO_2 + NO_3 \rightarrow N_2O_5$	(Vilà-Guerau de Arellano, 2015)
R25	$N_2O_5 \rightarrow NO_3 + NO_2$	(Vilà-Guerau de Arellano, 2015)
R26	$N_2O_5 + H_2O \rightarrow 2HNO_3$	$2.50 \cdot 10^{-22}$
R27	$N_2O_5 + 2H_2O \rightarrow 2HNO_3 + (H_2O)$	(Vilà-Guerau de Arellano, 2015)
	Monoterpene runs only	
R28	$MON + HO \rightarrow TPO_2$	$8.19 \cdot 10^{-11}$ / $5.33 \cdot 10^{-11}$ [b]
R29	$MON + O_3 \rightarrow 2MVK + 0.1HO_2 + 0.7HO$	$1.82 \cdot 10^{-16}$ / $8.09 \cdot 10^{-17}$ [b]
R30	$MON + NO_3 \rightarrow TPO_2$	$1.17 \cdot 10^{-11}$ / $6.16 \cdot 10^{-12}$ [b]
R31	$TPO_2 + NO \rightarrow 2MVK + HO_2 + HO$	$4.20 \cdot 10^{-12} \cdot e^{\frac{180}{T}}$
R32	$TPO_2 + HO_2 \rightarrow TPOOH$	$7.50 \cdot 10^{-13} \cdot e^{\frac{700}{T}}$
R33	$TPOOH + HO \rightarrow TPO_2$	$3.80 \cdot 10^{-12} \cdot e^{\frac{200}{T}}$
R34	$TPOOH + h\nu \rightarrow 2MVK + HO_2 + HO$	$3.01 \cdot 10^{-5} \cdot e^{\frac{-0.575}{\chi}}$

[a] First order reaction rates are in s^{-1}, second order reaction rates are in $cm^3 molec^{-1} s^{-1}$.
χ is the solar zenith angle and T [K] is the absolute temperature from the LES.

[b] Brackets indicate that the reaction scheme does not change the concentration of the species

[c] The first reaction rate is for an average monoterpene, while the second rate is for α-pinene only.

Kinematic heat fluxes

Observed kinematic heat fluxes at the study site were used to specify the canopy heat source in the simulation. Small differences between modeled and observed fluxes originated from smoothing and interpolation in the forcing data (Figure S1). The kinematic fluxes increased until about 10:30 h, with a marked decay at 11:00 h when clouds reduced the incoming sunlight (Figure S1a). Above the forest canopy and within the roughness sublayer, for the most part the kinematic fluxes remained invariant with height (Figure S1b). Above the rainforest roughness sublayer, the kinematic heat fluxes linearly decreased with altitude as typically observed in the convective boundary layer, reaching negative values some distance within the entrainment zone (Figure S1c).

Atmospheric turbulence

Atmospheric turbulence statistics, derived from the LES outputs, were contrasted with observed quantities for 21 September 2014 (Figure S2) to verify the fidelity of simulations in determining vertical velocity (w) and momentum transfer ($\overline{u'w'}$) as a function of height (z) normalized to canopy depth (z h_c^{-1}). Results (Figure S2) demonstrated that the numerical model realistically represented the air turbulence characteristics in and above the forest canopy. On average, the numerical simulations of the normalized mean velocity as a function of height ($\overline{u}$(z)) to the mean wind speed at h_c, $\frac{\overline{u}(z)}{u(h_c)}$, closely matched the observations in and above the forest canopy (Figure S2a). In the case of the standard deviation of the zonal wind speed (σ_u) normalized to the friction velocity (u_*), $\frac{\sigma_u(z)}{u_*)}$, the LES results agreed reasonably well in the canopy but above the forest the numerical model underestimated the $\frac{\sigma_u(z)}{u_*)}$ values (Figure S2b). Similar results were observed for vertical velocity variance $\frac{\sigma_w(z)}{u_*)}$ (Figure S2e). This discrepancy likely resulted from the assumption of flat topography or from the grid resolution adopted (or a combination of both). Simulations including topography under neutral stability conditions using a finer grid were in better agreement with observations from the same field campaign (Chen et al., 2019). The LES results and measured values of the skewness of the u, (Sk_u), showed qualitative good agreement in shape and depth, albeit with a reduced magnitude (Figure S2c). The results could be used as an indicator of the penetration depth of coherent sweeps and ejections. The penetration depth of sweeps and ejections occurred in

the upper half of the canopy. Results appeared to be in agreement with previous findings (Kruijt et al.,2000). Results for the momentum flux $\overline{u'w'}$ (Figure S2d) exhibited better agreement with observations and provided confidence that turbulent transport in the LES was realistically simulated and warranted reliable subsequent analyses of trace gas transport and chemistry in and above the forest canopy. There was also qualitative agreement between measurements and LES results for the skewness of vertical velocity (Sk_w), as both have a tendency for positive values above the canopy and for negative values below canopy height (Figure Sf).

Thermodynamics of the atmospheric boundary layer

After sunrise, canopy heating contributed to the growth of the convective boundary layer that reached a depth of 760 m around 12::00 hours (Figures S3a, b). After 7:00 h, the growth rate of the convective boundary remained approximately constant and started to slow after kinematic fluxes decreased after 11:00 h. Entertainment of drier air into the convective atmospheric boundary layer, initially decreased the specific humidity until the value stabilizes resulting from increased evapotranspiration (Figure S3c,d). The development of depth of the convective boundary layer and turbulent transport of kinematic heat appeared realistic (Figure S3a, b). There were no direct observations of temperature profiles at the study site to discern the depth of the mixed layer. Earlier studies (Fisch et al., 2004) observed boundary layer depths of 491 $\pm$ 133 m and 813 $\pm$ 128 m for 11:00 h and 14:00 h, respectively, over a rainforest site 24 km away from the study site during the wet season. The maximum boundary layer depth of 1002 $\pm$ 195 was observed around 17:00 h (Fisch et al., 2004).

Figure captions

Figure S1. Comparison of modeled and observed kinematic heat flux. a) Time series of kinemaic heat flux determined at canopy top (h_c). b) Hourly kinematic heat flux variations with normalized altitude (z h_c^{-1}). c) Hourly kinematic heat flux variations with z h_c^{-1} for the total vertical LES domain. Crosses indicate measured quantities while lines represent LES results.

Figure S2. Comparison of simulated (lines) and observed (crosses) atmospheric turbulence statis-

tics as a function of normalized height (z h_c^{-1}). a) Average zonal wind speed (u), (b) zonal wind speed standard deviation (σ_u), (c) zonal wind speed skewness (Sk_u), (d) vertical momentum transfer($\overline{u'w'}$), (e) vertical wind speed standard deviation (σ_w), and (f) vertical wind speed skewness (Sk_w). Turbulence statistics were hourly values from 7:00 h (yellow) to 12:00 h (dark red).

Figure S3. a) Contours of horizontally averaged virtual potential temperature ($\langle\tilde{\theta_V}\rangle$). b) Vertical variation of $\langle\tilde{\theta_V}\rangle$ for hours starting from 07:00 to 12:00 hours. c) Contours of horizontally averaged specific humidity ($\langle\tilde{q}\rangle$). d) Vertical variation of $\langle\tilde{q}\rangle$ for hours starting from 07:00 to 12:00 hours. The atmospheric convective boundary layer depth is indicated by black and red lines.

Appendix A. Figures

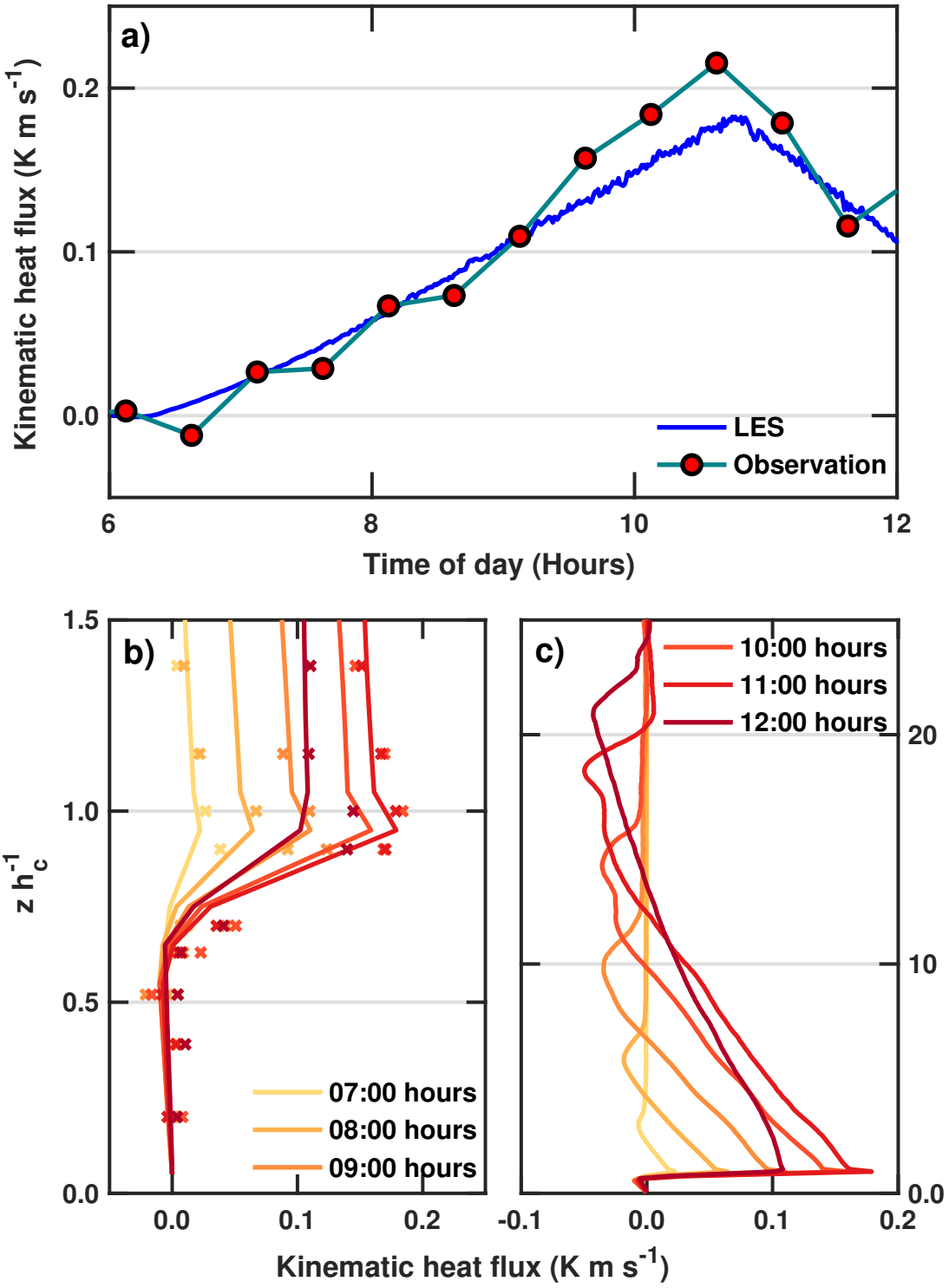
a)
Kinematic heat flux (K m s-1)
0.2
0.1
0.0
6
8
10
12
Time of day (Hours)
LES
Observation
b)
c)
z hc-1
1.5
1.0
0.5
0.0
07:00 hours
08:00 hours
09:00 hours
10:00 hours
11:00 hours
12:00 hours
20
10
0.0
-0.1
0.0
0.1
0.2
Kinematic heat flux (K m s-1)

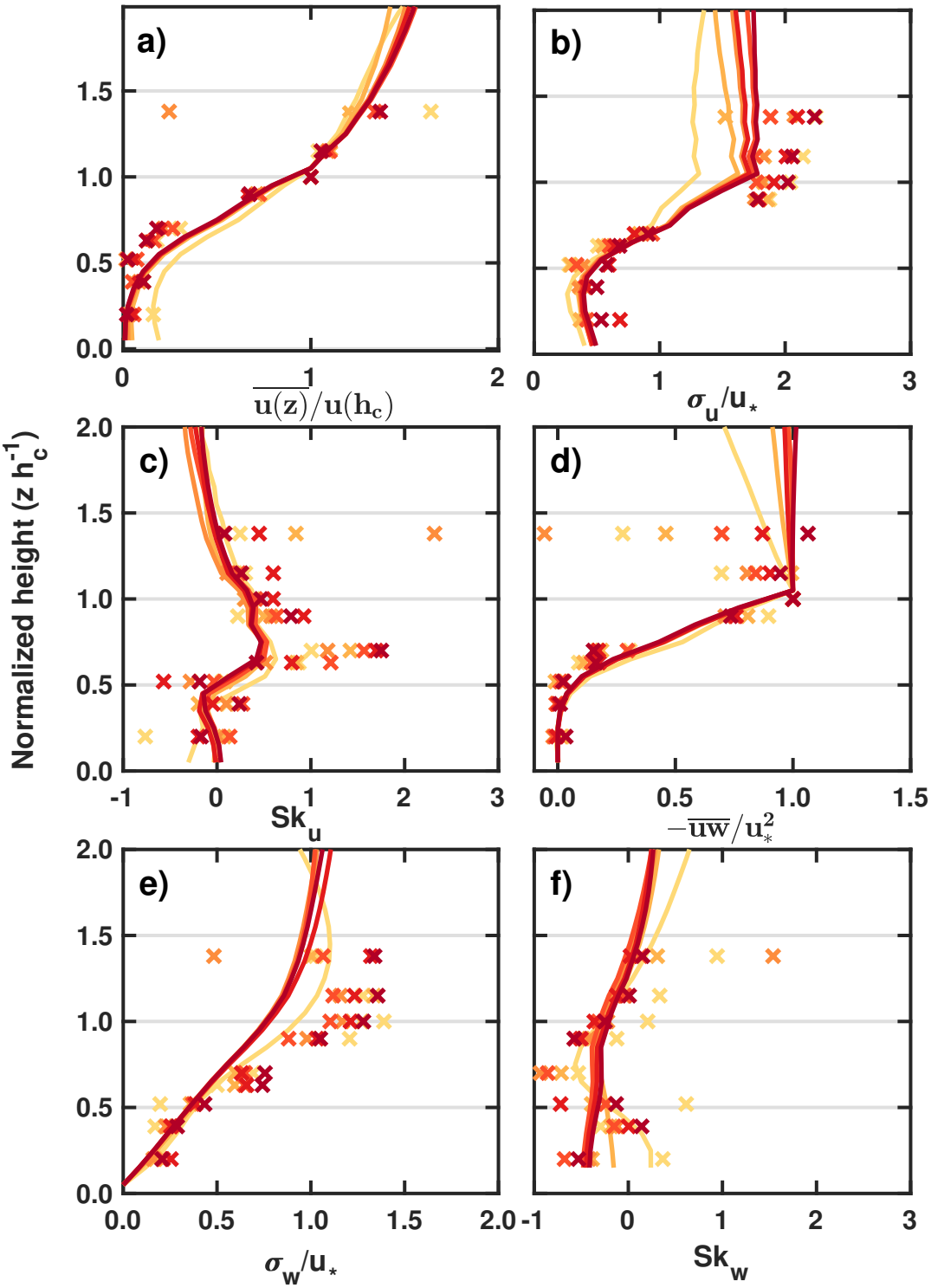
a)
b)
c)
d)
e)
f)
Normalized height (z h_c^-1)
$\overline{u(z)}/u(h_c)$
σ_u/u_*
Sk_u
$-\overline{uw}/u_*^2$
σ_w/u_*
Sk_w

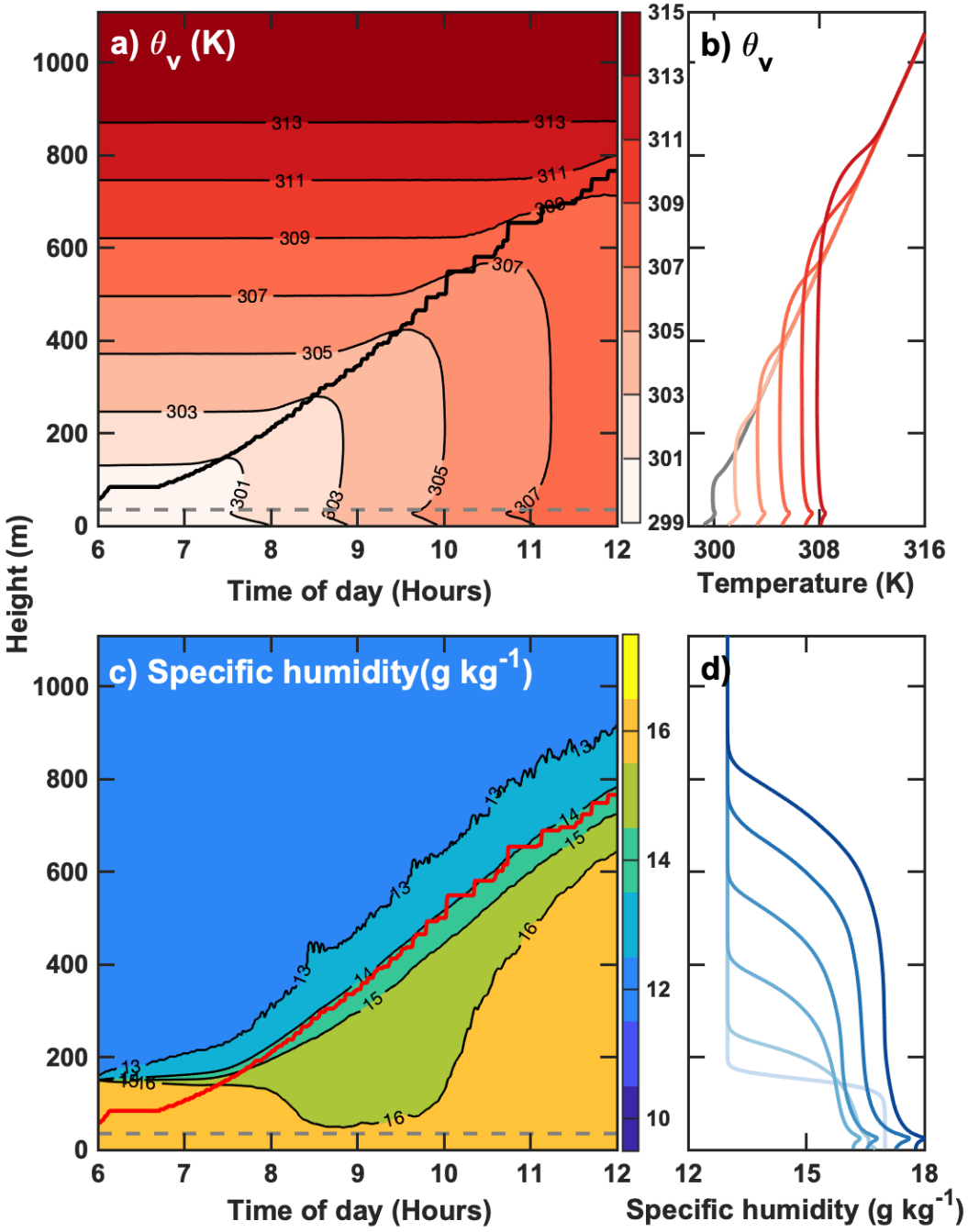

Figure Appendix A.3: Figure S3